

Chapter 1

Introduction

Chapter 2

Neutrino Physics

This chapter contains a introduction to the field of neutrino physics to provide context for the main work presented in this thesis. The history of neutrino physics is an interesting story in its own right and provides the foundation for the present and future of the field. This will be briefly retold in Section 2.1 and will motive a discussion of neutrino oscillations in Section 2.2. An overview of the current status of the field and its future is contained in Section 2.3. As this thesis specifically concerns the DUNE experiment, a brief history and description of liquid argon TPCs is provided in Section 2.4 as a basis for future chapters.

2.1 Historical Context

2.1.1 Prediction of the Neutrino

The neutrino was first postulated in 1930 by Wolfgang Pauli [1] in order to account for an inconsistency in the theory of β -decay. In the apparent two-body decay

$$A \rightarrow B + e^-, \quad (2.1)$$

kinematically the electron must be emitted with an energy given by

$$E = \left(\frac{m_A^2 - m_B^2 + m_e^2}{2m_A} \right) c^2, \quad (2.2)$$

where m_α is the mass of particle α . This energy is fixed given the masses of the particles; it was observed however that the electron energy followed a distribution (Figure 2.1), with Equation 2.2 giving the maximum permitted energy. The neutrino was postulated as a third final state particle in order to account for this result and retain energy conservation laws.

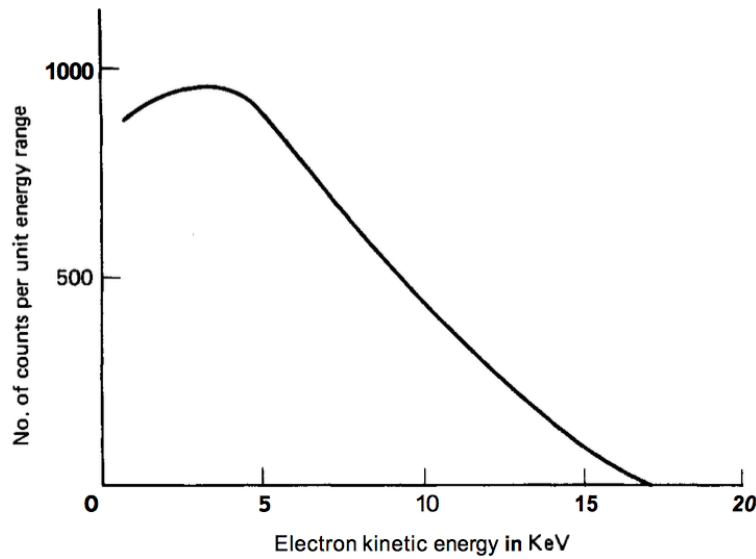


Fig. 2.1 Energy spectrum of the electron produced in beta decay [5].

Pauli initially called the particle a *neutron* (preempting the name Chadwick was to give his discovered particle in 1932) but his idea was met with much scepticism. It was Fermi who named the new particle *neutrino* ('little neutral one') when incorporating Pauli's hypothesis into his theory of beta decay [2–4]. With the huge success and acceptance of this theory, the field of neutrino physics was born.

Further indications of the existence of the neutrino were provided by the studies of pion and muon decay by Cecil Powell's group at Bristol in 1947 [6, 7]. Topological investigations of the newly discovered π meson and its apparent decay into a lighter meson (now known to actually be the muon lepton) appear to hint at the presence of an additional, unknown, daughter particle [6]. Furthermore, subsequent studies of the decay of the muons implied a three-body decay involving two unknown final state particles, analogous to the implication of the neutrino in β -decay by considering the electron energy distribution [8]. It seemed an model involving neutrinos could explain these observations and provided more suggestions for the existence of such a particle.

2.1.2 Discovery of the Neutrino

The elegance of Fermi's theory convinced many physicists of the existence of the neutrino but until discovered experimentally it remained a hypothetical 'book-keeping' device. Given the elusive nature of neutrinos this was not for many years, leading to Pauli famously declaring "I have done a terrible thing. I have postulated a particle that cannot be detected". However, a series of experiments conducted between 1953 and 1956 by Clyde Cowan and Frederick

Reines confirmed the hypothesis and was later rewarded with the Nobel Prize in Physics in 1995. Using the new technology of liquid scintillator detectors [9], they designed an experiment [10] to study the (anti)neutrinos produced in inverse beta decay

$$\bar{\nu}_e + p \rightarrow e^+ + n \quad (2.3)$$

in the Hanford nuclear reactor in Washington, U.S.A. Their signal comprised of an initial release of scintillation light when the positron annihilates with an electron, followed a characteristic time later by a gamma ray corresponding to the neutron capture. The initial results from 1953 [11] hinted at an excess over predicted background but the background proved to be much larger than anticipated, mainly due to an underestimation of the effects of cosmic rays. A second experiment was conducted in 1956, this time 12 m underground and 11 m from the Savannah River reactor in South Carolina. A neutrino detection rate of 2.9 ± 0.2 per hour, greater than 20 times the accidental background rate was reported, confirming the previous indications [12]. The experimental discovery of the neutrino was confirmed. [Bit more description? – Describe detector, method for detecting positron.]

Ray Davis was also using nuclear reactors to study the interaction rates of neutrinos. Using a detector comprised of 3000 gallons of carbon tetrachloride (CCl_4) also close to the Savannah River reactor, Davis and Harmer searched for the interactions

$$\bar{\nu} + \text{Cl}^{37} \rightarrow \text{Ar}^{37} + e^- \quad (\bar{\nu} + n \rightarrow p^+ + e^-). \quad (2.4)$$

Since it was known from Reines and Cowan that inverse beta decay

$$\nu + \text{Cl}^{37} \rightarrow \text{Ar}^{37} + e^- \quad (\nu + n \rightarrow p^+ + e^-) \quad (2.5)$$

occurs, this facilitated a comparison between the neutrino and the antineutrino. They found the interaction shown in Equation 2.4 occurred at a rate less than 20 times that represented in Equation 2.5, implying for the first time a difference between neutrinos and antineutrinos [13]. This gave rise to the notion of ‘lepton number’ and its conservation in physical interactions.

It was few years before the next chapter in the history of neutrinos, the discovery of the muon neutrino in 1962 at Brookhaven [14]. It was noted the apparently permitted decay

$$\mu^- \not\rightarrow e^- + \gamma \quad (2.6)$$

is never observed, inciting the possibility of two distinct neutrinos. In order to test this, Lederman, Schwarz and Steinberger used a muon neutrino beam to look for two separate

interactions:

$$\bar{\nu}_\mu + p^+ \rightarrow \mu^+ + n, \quad (2.7)$$

$$\bar{\nu}_\mu + p^+ \rightarrow e^+ + n. \quad (2.8)$$

With only one type of neutrino, each interaction would be expected to occur at around the same rate. The beam was produced by accelerating protons up to 15 GeV and using a Beryllium target to create secondary mesons, decaying to produce neutrinos with energies up to 1 GeV. 34 muon tracks were detected (with an estimated background from cosmic muons of 5) and no events consistent with electrons were observed. This remarkable result can only be rivalled by the technological advancements required; it was the first experiment to construct and use an artificial neutrino beam (common to all contemporary long-baseline experiments) and used 13.5 m thick steel from a dismantled battleship in order to ensure only neutrinos arrived at the spark chamber detector. This discovery was rewarded with the Nobel Prize in 1988.

A third generation of lepton, the τ , was discovered in 1975 by Martin Perl and his team at SLAC [15], completing the set of three charged leptons. They reported 64 events of the form

$$e^+ + e^- \rightarrow e^\pm + \mu^\mp + \geq 2 \text{ undetected particles}, \quad (2.9)$$

using the energy and angle distributions to predict at least two additional particles. They claimed ‘no conventional explanation’ could account for these events and proposed the existence of a heavier charged lepton as an intermediate stage:

$$e^+ + e^- \rightarrow \tau^+ + \tau^- \rightarrow e^\pm + \mu^\mp + 4\nu. \quad (2.10)$$

The τ lepton was subsequently characterised by further experiments by the Mark I detector at SLAC [16] and by the PLUTO collaboration at DESY [17]. This result heavily implied the existence of an associated neutrino to complete the symmetry observed in the first two lepton couplets.

Further evidence for a third neutrino was provided by four experiments using the Large Electron-Positron Collider (LEP) at CERN in 1989 which were studying the production of the newly discovered Z^0 boson [18–21]. The width Γ_Z of the Z^0 resonance is dependent on the partial widths relating to final state charged leptons, hadrons and neutrinos;

$$\Gamma_Z = N_\nu \Gamma_\nu + 3\Gamma_{ee} + \Gamma_{\text{hadron}}, \quad (2.11)$$

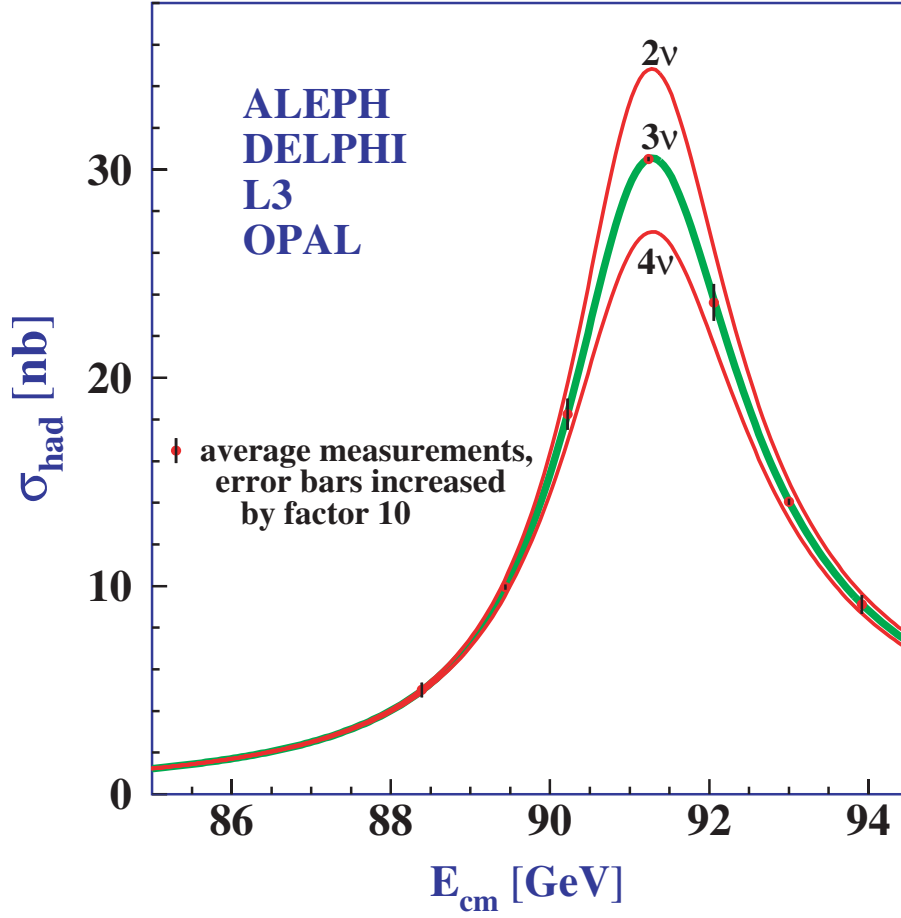


Fig. 2.2 Measurements of the hadron production cross-section around the Z resonance. The curves indicate the predicted cross-section for two, three and four neutrino species with SM couplings and negligible mass. Taken from [22].

where N_ν is the number of light ($m_\nu \leq \frac{m_Z}{2}$) active neutrinos. Figure 2.2 shows this resonance for a range of N_ν hypotheses; fitting to the data yields a value of 2.984 ± 0.008 neutrino flavours [22].

The extremely precise measurement reported by the LEP experiments was enough for a lot of physicists to claim indisputable evidence for the existence of the tau neutrino; it was partly for this reason that its experimental discovery was not until 25 years after the addition of the τ lepton to the Standard Model. However, in 2000 the DONUT experiment at Fermilab, IL, U.S.A. finally reported direct detection of the tau neutrino [23]. As its name suggests, DONUT (Direct Observation of NuTau) was designed specifically for the purpose of finding the third neutrino. It did this by identifying the τ as the only lepton at the interaction vertex from a ν_τ beam created by firing 800 GeV protons from the Tevatron at a tungsten beam dump. The mean energy of the ν_τ s detected at the emulsion target 36 m downstream was

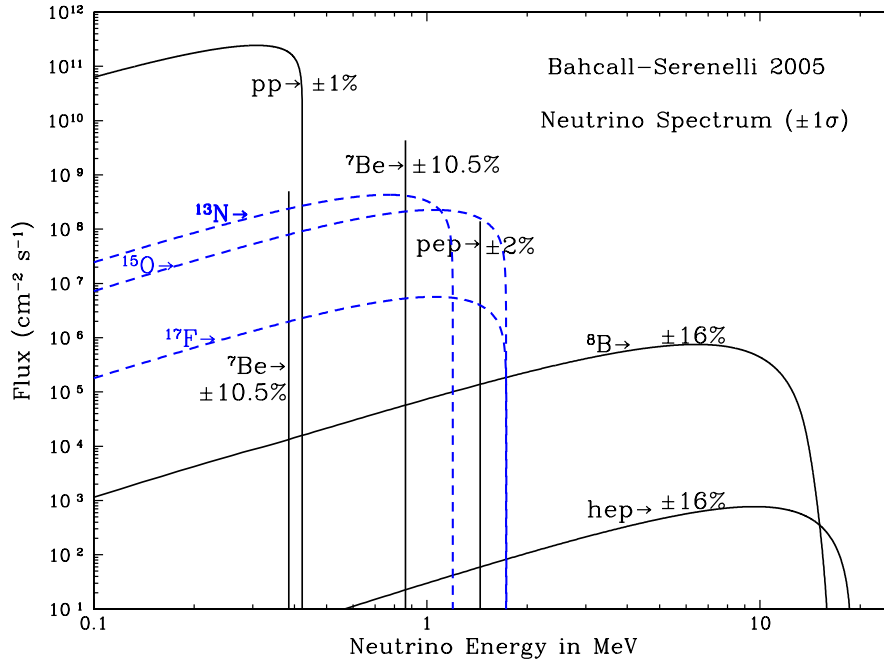


Fig. 2.3 Solar neutrino energy spectra as predicted by the Standard Solar Model [26]. The solid lines represent neutrinos produced during the p-p chain and dashed line represent neutrinos from the CNO cycle. Each spectrum illustrates a particular reaction during the process of a given chain.

111 GeV, produced by the decay of a D_S meson to a τ lepton and a $\bar{\nu}_\tau$ neutrino followed by the decay of the τ to a ν_τ . Four events were found, above a predicted background of 0.34 ± 0.05 , consistent with the Standard Model description of the tau neutrino.

2.1.3 The Solar Neutrino Problem

It has been known since the 1930s, when Hans Bethe started developing the ideas of stellar nucleosynthesis [24], that an abundance of electron neutrinos is created as byproducts of the nuclear processes powering the Sun. The Standard Solar Model (SSM), established by John Bahcall in 1968 [25], explains the nuclear fusion processes responsible for powering stars. For stars the size of the Sun, this is dominated by the *proton-proton chain*; heavier stars follow the *CNO cycle*. Figure 2.3 shows the energy spectra of neutrino released during reactions occurring during both chains.

Ray Davis, in collaboration with Bahcall, conducted the first experiment to detect these solar neutrinos in 1968. Using a similar detection technique to his previous experiments, Davis used a 380 m³ tank of tetrachloroethene (C₂Cl₄) to detect neutrinos via the inverse beta decay reaction detailed in Equation 2.5. Given the threshold for this reaction is 0.814 MeV, the

main sources of neutrinos probed by this experiment were Be^7 and B^8 . In order to eliminate backgrounds from cosmic rays, Davis constructed his experiment 4850 ft underground at the Homestake mine near Lead, SK, U.S.A. It is worth noting, in a pleasing neutrino-full-circle, this is exactly where the far detector for the DUNE experiment will be housed. The Davis Homestake experiment ran for 25 years but the results obtained [27] disagreed quite strongly with the SSM [28], consistently measuring solar electron neutrinos at a rate around a third that predicted by the model. This became known as the ‘solar neutrino problem’, and Davis was awarded the Nobel Prize for his work on this famous experiment in 2002.

The subsequent radiochemical experiments SAGE (from 1990) and GALLEX (from 1991) were sensitive to the large flux of pp neutrinos by utilising a Ga^{71} target and the lower threshold reaction

$$\nu + \text{Ga}^{71} \rightarrow \text{Ge}^{71} + e^{-}. \quad (2.12)$$

These experiments also reported ‘missing’ neutrinos, determining capture rates of $66.6^{+6.8+3.8}_{-7.1-4.0}$ SNU (SAGE) [29] and $77.5 \pm 6.2^{+4.3}_{-4.7}$ SNU (GALLEX) [30], disagreeing with the SSM prediction of 130 SNU [31]. There appeared to be a problem – either the SSM was incomplete and incorrectly over-predicted the amount of electron neutrinos or hints of new physics were beginning to appear in the experiment data.

2.1.4 The Atmospheric Neutrino Anomaly

Another abundant source of natural neutrinos come from cosmic rays interacting with the upper atmosphere and producing ‘atmospheric neutrinos’, typically via the interactions [32]

$$\pi^{+} \rightarrow \mu^{+} + \nu_{\mu}, \quad \mu^{-} \rightarrow e^{-} + \bar{\nu}_e + \nu_{\mu} \quad (2.13)$$

$$\pi^{-} \rightarrow \mu^{-} + \bar{\nu}_{\mu}, \quad \mu^{+} \rightarrow e^{+} + \nu_e + \bar{\nu}_{\mu}. \quad (2.14)$$

Since the decay lengths and kinematics are well known, the predicted ratio of muon to electron neutrinos can be calculated to a good accuracy. This ratio can be compared to an experimentally determined ratio and analysed as a measure of the efficacy of the model.

It was first noticed as early as the late 1970s by experiments designed to search for nucleon decay predicted by the then-popular Grand Unified Theories that the measured flux did not correspond to that predicted by the theory. The IMB [33] and Kamioka [34] experiments, whilst measuring the atmospheric neutrino flux as an important background for nucleon decay, both noticed deficiencies in the ratio between muon and electron neutrinos compared to that predicted by the models. These experiments utilised large tanks of pure water surrounded by Photo-Multiplier Tubes (PMTs) to detect neutrinos via the Cherenkov

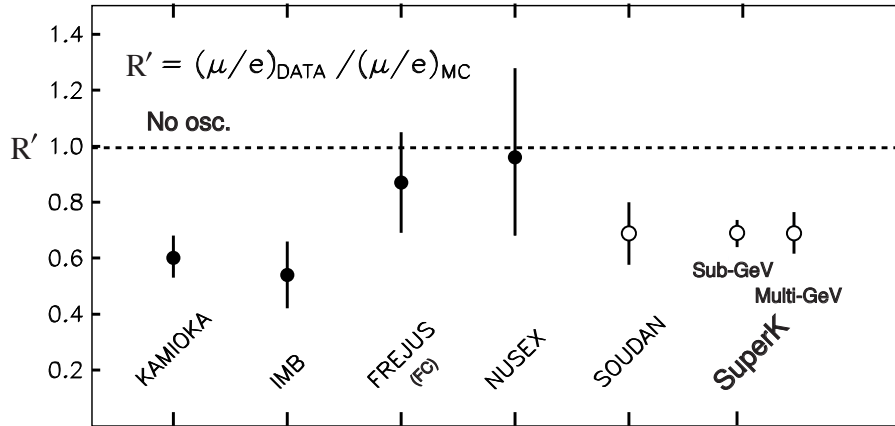


Fig. 2.4 The double ratio R of muon to electron neutrino events showing data divided by expectation [35]. Various underground atmospheric neutrino detectors are shown.

radiation created by their charged leptonic daughter particles. Using ring-imaging techniques, it is possible to distinguish between electron-like and muon-like events and therefore identify the flavour of the incoming neutrino. The problem implied by these measurements is known as the ‘atmospheric neutrino anomaly’.

Various other experiments over the following twenty years also reported similar measurements, suggesting an excess of electron neutrinos over prediction, a deficit in the number of muon neutrinos, or both. Results from numerous experiments are shown in Figure 2.4. Most experiments report a discrepancy, with its size seemingly dependent on the energy region being studied. The experiments reporting a ratio consistent with one were much smaller than the others, and with more statistics they also started observing similar effects. This anomaly, along with the issue of the solar neutrino problem, strongly hinted at a problem with our understanding of neutrino physics. This is to be discussed in detail in the Section 2.2.

2.2 Neutrino Oscillations

The concept of neutrino oscillations involves the changing of the flavour of a neutrino as it propagates through time and space; a neutrino created in a certain flavour has a non-zero probability of being later detected in a different flavour state. It was first postulated as an explanation of the Solar Neutrino Problem by Pontecorvo in 1968 [36, 37], having initially proposed the phenomenon in 1957 as an analogy to $K^0 \rightarrow \bar{K}^0$ transition in the quark sector [38]. It offers an elegant solution to both the solar neutrino problem and the atmospheric neutrino anomaly by explaining where the ‘missing’ neutrinos had gone; it is possible they had simply ‘oscillated’ to a different flavour and therefore would not be detected as expected.

2.2.1 The Evidence for Neutrino Oscillations

Whilst there was speculation that neutrino oscillations may be the explanation behind the issues observed in the data much sooner [39, 40], definite proof was not provided until the late 1990s. In many ways, the story of neutrino physics, from the initial observations of the Solar Neutrino Problem and the Atmospheric Neutrino Anomaly, through the speculation and theoretical developments, to the eventual proof, can be considered a triumph for the scientific method.

The Kamiokande and Super-Kamiokande experiments in Japan (upgrades from the Kamioka experiment noted previously) and the SNO experiment in Sudbury, Canada produced the results which showed indisputable evidence for neutrino oscillations and provided explanations for all previous discrepancies observed. This result was monumental and the work of both collaborations was rewarded in 2015 when the Nobel Prize was awarded to T. Kajita and A. McDonald, from Super-Kamiokande and SNO respectively.

2.2.1.1 Super-Kamiokande and the Atmospheric Sector

In 1994, the Kamiokande experiment produced results which hinted at an angular dependence for the R -ratio deficit, implying a dependence on neutrino travel distance [41]. This result can be explained by invoking neutrino oscillations since the probability of oscillation is influenced by the propagation distance; its significantly larger successor, Super-Kamiokande, was constructed in order to make precise measurements of this phenomenon. Super-Kamiokande is located 1000 m underground and contains an inner detector consisting of 22.5 kton fiducial volume of pure water contained within a large stainless steel cylinder (37 m high, 34 m diameter) and surrounded by 13 142 20-inch photo-multipliers. With 40% coverage, the photocathodes extended over nearly an acre and provided ten times more pixels than any other experiment at the time. Its results in 1998 confirmed the earlier angular dependence findings of Kamiokande, Figure 2.5, and also considered the data as a function of neutrino energy and propagation distance, as shown in Figure 2.6. The observed effects disagreed with a view of non-oscillating atmospheric neutrinos but were entirely consistent with a two-flavour oscillation model, $\nu_\mu \rightarrow \nu_\tau$. This resulted in the famous published claim for the experimental discovery of neutrino oscillations [42].

2.2.1.2 SNO and the Solar Sector

After the Super-Kamiokande results, it was clear that neutrino oscillations would probably also explain the deficit of electron neutrinos observed by solar neutrino experiments. It took

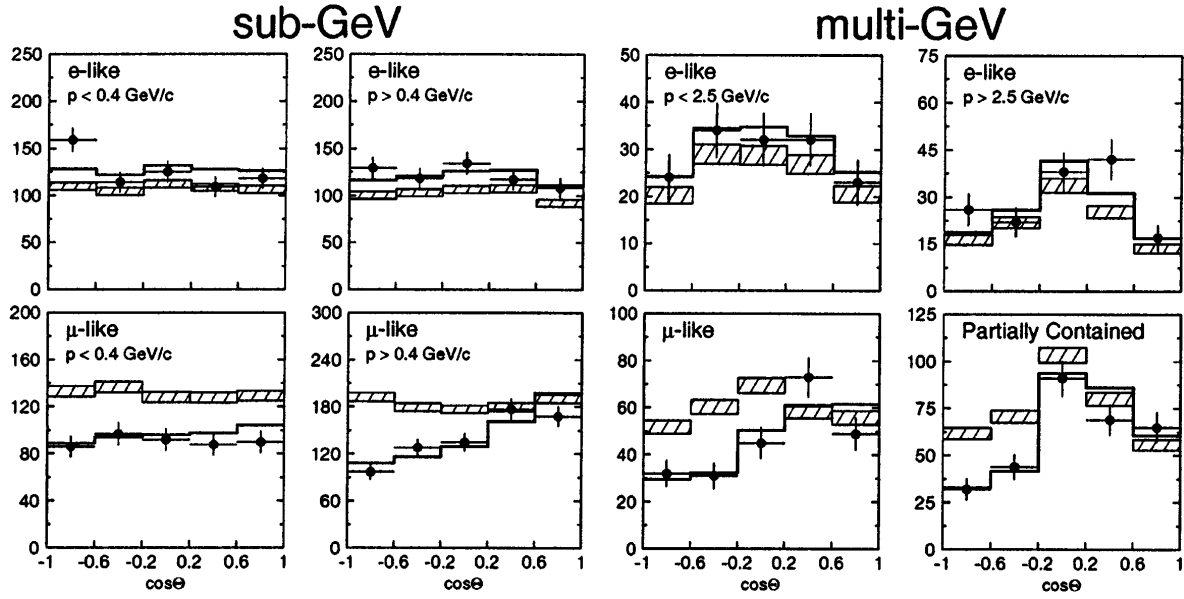


Fig. 2.5 Zenith angle distributions of μ -like and e -like events for sub-GeV and multi-GeV data sets. Upward-going particles have $\cos \Theta < 0$ and downward-going particles have $\cos \Theta > 0$. The hatched region shows the Monte Carlo expectation for no oscillations and the bold line is the best-fit expectation for $\nu_\mu \rightarrow \nu_\tau$ oscillations. Taken from [42].

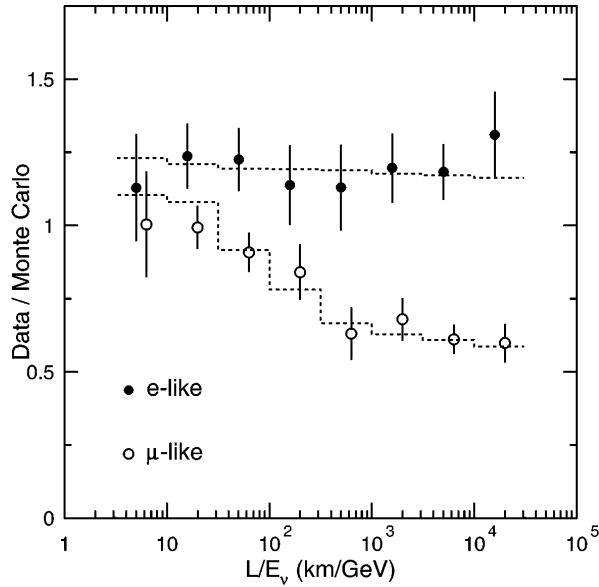


Fig. 2.6 The ratio of the number of data events to Monte Carlo events in the absence of oscillations as a function of reconstructed L/E_ν . The dashed lines show the expected shape for $\nu_\mu \rightarrow \nu_\tau$ oscillations. Taken from [42].

a few years until the Sudbury Neutrino Observatory (SNO) in Canada provided some quite brilliant evidence of this in 2002 [43].

SNO was a water Cherenkov detector, like Super-Kamiokande, but used heavy water (D_2O) as a detector medium. The water is contained in a 12 m acrylic spherical shell and surrounded by 9456 photomultipliers at a depth of 6010 m water equivalent. The use of heavy water facilitated sensitivity to other neutrino interaction channels not accessible by Super-Kamiokande via the charge current (CC), neutral current (NC) and elastic scattering (ES) interactions;

$$\nu_e + d \rightarrow p + p + e^- \quad (\text{CC}) \quad (2.15)$$

$$\nu_x + d \rightarrow p + n + \nu_x \quad (\text{NC}) \quad (2.16)$$

$$\nu_x + e^- \rightarrow \nu_x + e^- \quad (\text{ES}). \quad (2.17)$$

The CC channel is sensitive exclusively to electron neutrinos, whilst the other two are accessible by neutrinos of any flavour. This allowed for the first time a simultaneous measurement of the total neutrino interaction rate as well as the electron neutrino interaction rate. The observations of SNO were the smoking gun for neutrino oscillations; the total measured flux for all neutrinos, $\phi_{\text{NC}}^{\text{SNO}} = 6.42 \pm 1.57 \text{ (stat.)}_{-0.58}^{+0.55} \text{ (sys.)}$, agreed excellently with the electron neutrino flux predicted by the SSM, $\phi^{\text{SSM}} = 5.05_{-0.81}^{+1.01}$. However, the measured electron neutrino flux was around a third lower, $\phi_e^{\text{SNO}} = 1.76 \pm 0.05 \text{ (stat.)} \pm 0.09 \text{ (sys.)}$, consistent with previous measurements from the radiochemical experiments. The evidence seems conclusive: the solar models are correct and the neutrinos are not disappearing; there are simply changing their flavour state. A summary plot showing all solar neutrino experiments up until this point is shown in Figure 2.7 [44].

2.2.2 Vacuum Oscillations

The theory of neutrino oscillations is basically the quantum mechanics of mixed states and was developed on top of Pontecorvo's work by Ziro Maki, Masami Nakagawa and Shoichi Sakata [45]. If the neutrino flavour states can spontaneously convert from one to another, none can be considered as eigenfunctions of the Hamiltonian. The true stationary states are the *mass eigenstates* (ν_1, ν_2, ν_3), of which the flavour states (ν_e, ν_μ, ν_τ) can be considered linear superpositions:

$$\begin{pmatrix} \nu_e \\ \nu_\mu \\ \nu_\tau \end{pmatrix} = U_{\text{PMNS}}^* \begin{pmatrix} \nu_1 \\ \nu_2 \\ \nu_3 \end{pmatrix}, \quad (2.18)$$

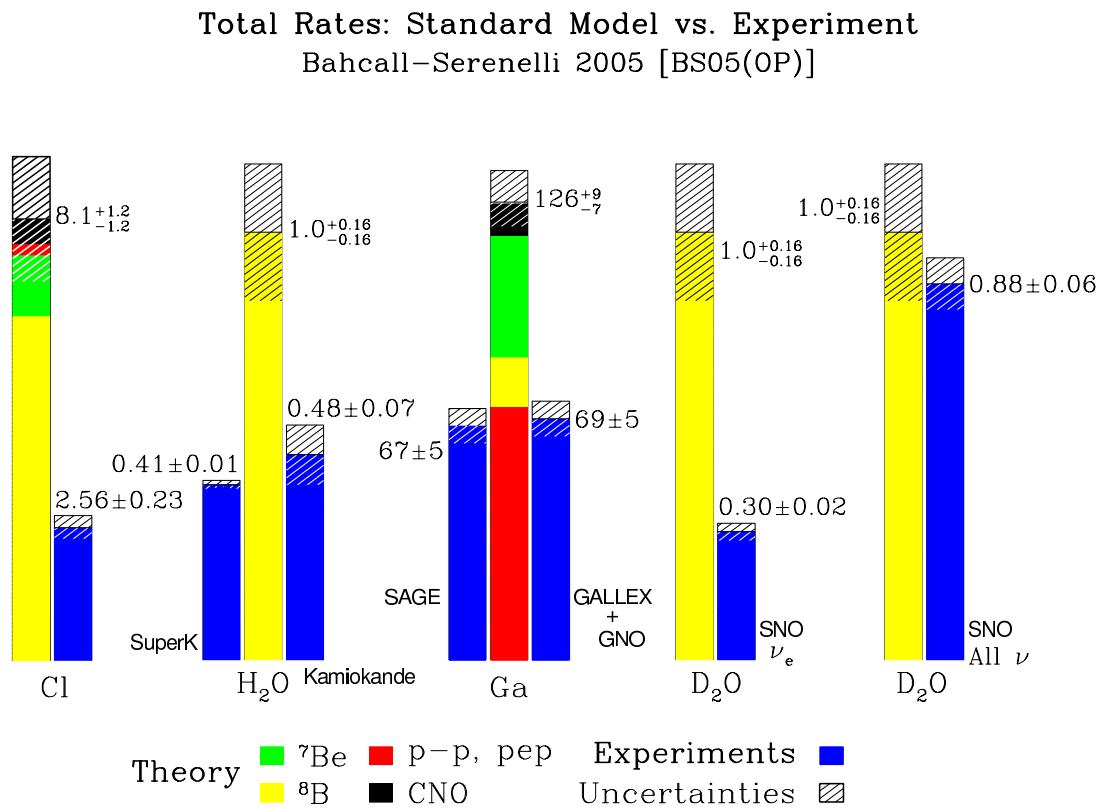


Fig. 2.7 Comparison of the predictions of the neutrino fluxes from the Standard Solar Model with measured rates from a variety of solar neutrino experiments. The results of SNO (D₂O target, right two comparisons) show that the expected flux is observed, but not necessarily as electron neutrinos. This shows conclusively the oscillatory nature of neutrinos.

where U_{PMNS} is the PMNS mixing matrix which described the flavour composition of each of the mass eigenstates, and vice versa. If the PMNS matrix were diagonal, each flavour state would correspond to a single mass state and oscillations would not occur.

Just as the flavour states are a superposition of mass states

$$|v_\alpha\rangle = \sum_i U_{\alpha i}^* |v_i\rangle, \quad (2.19)$$

the mass states can also be considered a superposition of flavour states

$$|v_i\rangle = \sum_\alpha U_{\alpha i} |v_\alpha\rangle. \quad (2.20)$$

For the three neutrino case, the PMNS matrix, decomposed into its three axial rotations, can be expressed as

$$U_{\alpha i} \equiv \underbrace{\begin{pmatrix} 1 & 0 & 0 \\ 0 & c_{23} & s_{23} \\ 0 & -s_{23} & c_{23} \end{pmatrix}}_{\text{'Atmospheric' term}} \underbrace{\begin{pmatrix} c_{13} & 0 & e^{-i\delta}s_{13} \\ 0 & 1 & 0 \\ -e^{-i\delta}s_{13} & 0 & c_{13} \end{pmatrix}}_{\text{'Accelerator' or 'Reactor' term}} \underbrace{\begin{pmatrix} c_{12} & s_{12} & 0 \\ -s_{12} & c_{12} & 0 \\ 0 & 0 & 1 \end{pmatrix}}_{\text{'Solar' term}}, \quad (2.21)$$

where $c_{ij} \equiv \cos(ij)$, $s_{ij} \equiv \sin(ij)$ and δ is a CP-violating phase factor. Each axial component is often referred to by the means with which they are studied, as shown in Equation 2.21.

The weak interaction couples to the flavour eigenstates so neutrinos are always created and detected as flavour states. However, they propagate as mass states since it is these which are eigenstates of the Hamiltonian. Due to the misalignment of the flavour and mass states, oscillations can be shown to occur. A neutrino created with flavour α is a superposition of all the mass states (Equation 2.19). These states propagate as a plane wave, evolving in time and space such that

$$|v_i(x, t)\rangle = |v_i(0)\rangle e^{-i\mathbf{x}\cdot\mathbf{p}}, \quad (2.22)$$

where \mathbf{x} and \mathbf{p} are the 4-position and 4-momentum of the neutrino respectively. From Equations 2.19 and 2.22, the evolution of the flavour states over space and time is therefore

$$\begin{aligned} |v_\alpha(x, t)\rangle &= \sum_i U_{\alpha i}^* |v_i(x, t)\rangle \\ &= \sum_i U_{\alpha i}^* e^{-i\mathbf{x}\cdot\mathbf{p}} |v_i(0)\rangle. \end{aligned} \quad (2.23)$$

In the ultra-relativistic limit, the mass of the neutrino is negligible compared to its momentum ($m_i \ll \vec{p}$) and $\vec{x} \approx ct$;

$$E_i = \sqrt{|\vec{p}|^2 + m_i^2} = \vec{p} \sqrt{1 + \frac{m_i^2}{|\vec{p}|^2}} \approx \vec{p} + \frac{m_i^2}{2\vec{p}} \quad (2.24)$$

$$\mathbf{x} \cdot \mathbf{p} = E_i t - \vec{x} \cdot \vec{p} = \vec{p} \cdot t + \frac{m_i^2}{2\vec{p}} t - \vec{x} \cdot \vec{p} \approx \frac{m_i^2}{2\vec{p}} \vec{x} = \frac{m_i^2}{2p} x, \quad (2.25)$$

assuming the neutrino displacement is in the direction of its momentum and using natural units ($c \equiv \hbar \equiv 1$). Thus, using Equations 2.23, 2.25 and 2.20,

$$\begin{aligned} |\nu_\alpha(x, t)\rangle &= \sum_i U_{\alpha i}^* e^{-i \frac{m_i^2}{2p} x} |\nu_i(0)\rangle \\ &= \sum_i \sum_\beta U_{\alpha i}^* e^{-i \frac{m_i^2}{2p} x} U_{\beta i} |\nu_\beta\rangle. \end{aligned} \quad (2.26)$$

The probability of a neutrino created in flavour state α being observed in flavour β can be determined from Equation 2.26

$$P(\alpha \rightarrow \beta) = |\langle \nu_\alpha | \nu_\beta(x, t) \rangle|^2 \quad (2.27)$$

$$= \left[\sum_i U_{\alpha i} e^{i \frac{m_i^2}{2p} x} U_{\beta i}^* \right] \left[\sum_j U_{\alpha j}^* e^{-i \frac{m_j^2}{2p} x} U_{\beta j} \right] \quad (2.28)$$

$$= \sum_{i,j} U_{\alpha i} U_{\alpha j}^* U_{\beta j} U_{\beta i}^* e^{i \frac{m_i^2 - m_j^2}{2p} x}, \quad (2.29)$$

and is observed to be dependent on the neutrino momentum, the difference between the squared masses of the flavour states, the propagation distance and the relative mixing of the two flavour states encoded in the matrix elements U .

An accelerator based neutrino experiment, such as DUNE, will typically use a ν_μ -dominated beam and look for *muon neutrino disappearance* ($P(\nu_\mu \rightarrow \nu_\mu)$) and *electron neutrino appearance* ($P(\nu_\mu \rightarrow \nu_e)$). In this case, also in the relativistic limit, the relevant appearance and disappearance probabilities can be approximated, respectively, as

$$P(\nu_\mu \rightarrow \nu_e) \approx \sin^2 2\theta_{13} \sin^2 \theta_{23} \sin^2 \left(1.27 \frac{\Delta m_{13}^2 L}{E} \right) \quad (2.30)$$

$$P(\nu_\mu \rightarrow \nu_\mu) \approx 1 - \cos^4 \theta_{13} \sin^2 2\theta_{23} \sin^2 \left(1.27 \frac{\Delta m_{23}^2 L}{E} \right), \quad (2.31)$$

where $\Delta m_{ij}^2 \equiv m_i^2 - m_j^2$ is the *mass squared splitting* in eV, L is the distance propagated in km and E is the neutrino energy in GeV.

From these equations, it can be seen the important controllable parameters relevant for observing oscillations are the neutrino energy and the distance they travel. An experiment will typically chose a ratio L/E which will attempt to maximise the effect of oscillations in order to make precision measurements.

2.2.3 Matter Effects

The oscillations considered thus far are *vacuum oscillations* which occur due to the mixing of the neutrino mass and flavour states. Whilst directly confirming the oscillation of solar neutrinos, the SNO experiment (along with every other solar neutrino experiment) reported more oscillations than can be explained using just the vacuum oscillation model discussed in Section 2.2.2 [46, 47]. When neutrinos propagate through matter, an additional potential can be shown to also produce oscillations, which would occur even in the case of massless neutrinos (as long as mixing occurs). Since solar neutrinos travel through dense matter before exiting the Sun, it is possible these matter effects explained above could explain this discrepancy.

Coherent scattering (scattering in which the neutrino state is unchanged) due to interactions with the medium cause neutrinos travelling through matter to feel a potential. As normal matter is composed of electrons, rather than their heavier counterparts muons and taus, electron neutrinos are affected more by this potential. The mechanism for this is demonstrated in Figure 2.8. This gives rise to an additional effective mass splitting between the electron neutrino and the other flavours and therefore results in the possibility of oscillations [48]. Due to the density of the Sun and the neutrino energies, the neutrinos actually feel a resonance which causes their oscillation probability to become dramatically higher than the vacuum oscillation probabilities. This is known as the Mikheev-Smirnov-Wolfenstein (MSW) effect [49, 50].

2.2.3.1 KamLAND and Reactor Neutrinos

In order to investigate the possible MSW effects in the Sun, measurements of electron neutrino disappearance from terrestrial neutrinos, which were not subject to these matter effects, were considered. The first experiment to publish results was KamLAND (Kamioka Liquid Scintillator Anti-Neutrino Detector) in 2003 [51, 52]. KamLAND occupied the site previously used by the Kamiokande experiment in Japan under 2700 m.w.e of rock and utilised 1 kton of ultrapure liquid scintillator contained in a 13 m spherical balloon.

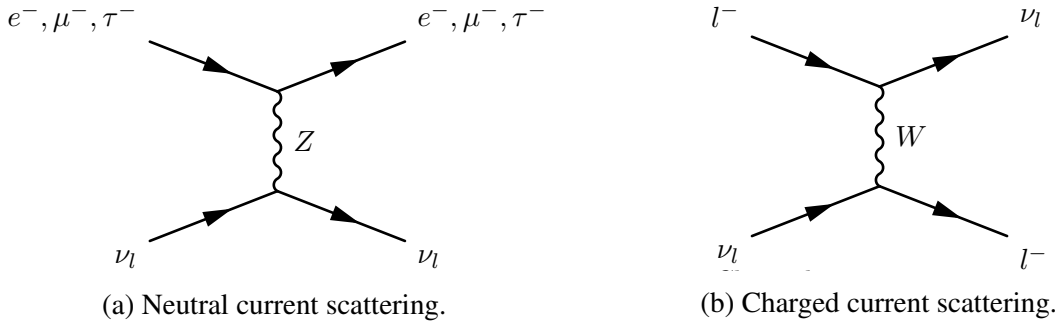


Fig. 2.8 General scattering mechanics which occur as neutrinos pass through matter. Neutral current scattering (Figure 2.8a) occurs for all neutrino flavour combinations whereas charged current scattering (Figure 2.8b) only occurs when the incoming leptons have the same flavour.

It was surrounded by 53 Japanese nuclear power reactors with baselines ranging from 80 km to 800 km and detected the $\bar{\nu}_e$ s via the inverse beta decay reaction $\bar{\nu}_e + p \rightarrow e^+ + n$. Scintillation light from the delayed coincidence of a positron with the neutron capture was detected using 1879 PMTs and constituted a signal with very low background. The results from KamLAND confirmed the apparently large matter effect in solar neutrinos and completely solved for the first time the long-standing Solar Neutrino Problem [53–55].

2.2.4 CP-Violation

The δ terms in Equation 2.21 are CP-violating phase factors. They could be included in any of the diagonalised components but are generally added to the accelerator part since this is how current and future experiments will look for evidence of CP-violation. As long as all the mixing angles are non-zero, there is the possibility of CP-violation in the lepton sector.

This is an exciting prospect and one of the reasons for the current intense interest in neutrino physics. It is known CP-violating processes must have occurred in the early Universe since matter has come to dominate massively over antimatter after they were created equally in the Big Bang. This has been observed in the quark sector but current experimental evidence can only account for a small amount of the necessary CP-violation. It is also expected but has never been observed in strong interactions [56]. Leptonic CP-violation could potentially account for the matter-antimatter asymmetry in the Universe and ultimately explain how it evolved to include our very existence [57, 58].

In neutrino experiments, effects of CP-violation would be apparent as a difference in behaviour between neutrinos and antineutrinos. For example, since the sign of δ is different

for neutrinos and antineutrinos, an asymmetry

$$\mathcal{A} = \frac{P(\nu_\mu \rightarrow \nu_e) - P(\bar{\nu}_\mu \rightarrow \bar{\nu}_e)}{P(\nu_\mu \rightarrow \nu_e) + P(\bar{\nu}_\mu \rightarrow \bar{\nu}_e)} \quad (2.32)$$

can be observed and measured.

2.3 Status of Neutrino Physics

The field of neutrino physics has advanced rapidly over the past twenty to thirty years (discussed in Sections 2.1 and 2.2) and there is currently a good understanding of most experimental results in the context of 3-flavour neutrino oscillations. Presently, the focus has shifted to making precise measurements of the oscillation parameters and trying to understand the nature of neutrino mass. The current understanding of each of these areas will be presented in Sections 2.3.2 and 2.3.3 respectively following a brief overview of current and future experiments in Section 2.3.1.

2.3.1 Current and Future Experiments

In recent years, neutrino experiments which utilise a custom built artificial neutrino beams have been offering complimentary and world-leading results. These ‘accelerator experiments’ are used in order to have more control over the energy spectrum and composition of the neutrino beam and often use a long-baseline, sampling the beam at different points to determine the effects of oscillation as the neutrinos propagate in between.

MINOS was based at Fermilab, U.S., and detected neutrinos from the NuMI (Neutrinos at the Main Injector) beam at a ‘near detector’ and then again in Northern Minnesota, a baseline of 735 km. T2K follows a similar design and uses the Super-Kamiokande detector as the far detector, utilising a beam from J-PARC, Japan and a baseline of 295 km. T2K and NOvA, another current long-baseline experiment, were designed specifically to measure the last mixing parameter, θ_{13} , by looking for ν_e appearance in a ν_μ beam. NOvA, like its predecessor MINOS, also uses the NuMI beam and has a far detector at the same site. However, along with T2K, it is ‘off-axis’ by around 2° ; this produces a more monotonic neutrino energy spectrum to maximise the effect of oscillations and make more accurate measurements. T2K and NOvA still have many years left of their respective programmes and are currently making precision measurements of the mixing parameters along with constraining CP-violation by combining neutrino and antineutrino analyses. They will not be

able to make statistically significant measurements of this area but, especially through joint analyses, will be able to offer hints before the next generation of experiments.

Future long-baseline experiments include DUNE [], which will be discussed properly in Chapter 3, and Hyper-Kamiokande [59], an upgrade of the current T2K experiment. Hyper-Kamiokande will also use water Cherenkov technology but will boast a fiducial volume 25 times larger than that of Super-Kamiokande. The timescale of these projects is on the order of at least ten years from now and both pose incredible engineering challenges in their own right.

2.3.2 Oscillation Parameters

The current status of the mixing angles and the mass-squared differences is depicted in Figure 2.9. The world-best measurements for θ_{12} and Δm_{12}^2 are provided by the solar neutrino experiments (Homestake [27], GALLEX [60], SAGE [61] and SNO [62]) and KamLAND [63]. The leading measurements in the atmospheric neutrino sector, θ_{23} and $|\Delta m_{32}^2|$, are from Super-Kamiokande [64], IceCube [65] and the accelerator experiments MINOS [66, 67], T2K [68] and NOvA [69].

The value of θ_{13} was known, from limits determined from global fits to world data, to be much smaller than the others and was even consistent with zero. In addition to the accelerator experiments, reactor neutrino experiments are also sensitive to θ_{13} via $\bar{\nu}_e$ disappearance and it was these experiments which produced the decisive results first. Daya Bay [72] in China and RENO [73] in South Korea found evidence of a non-zero value in 2012. There is good agreement between these reactor experiments and more recent measurements from T2K [74] and NOvA [75].

A summary of the best known values for all these oscillation parameters is shown in Table 2.1. The CP-violating phase δ_{CP} is currently unmeasured and provides a priority for current and future neutrino experiments. T2K have excluded the CP conservation regions with little statistical significance and currently favours a maximal CP-violation value of $\delta_{\text{CP}} = -\pi/2$ [76] [NOTE TO ME! Just preprint, may be published by the time I've finished writing this thing!]; this holds much promise for future experiments. The octant of θ_{23} , the location of the parameter in either the $> 45^\circ$ or $< 45^\circ$ octant, is also undetermined and requires high precision measurements; it is possible that the mixing in this sector is ‘maximal’ ($\theta_{23} = 45^\circ$).

2.3.3 Neutrino Mass

Neutrinos in the Standard Model are massless, for no real reason. However, the observation of neutrino oscillations implies the existence of neutrino mass (the oscillation probabilities,

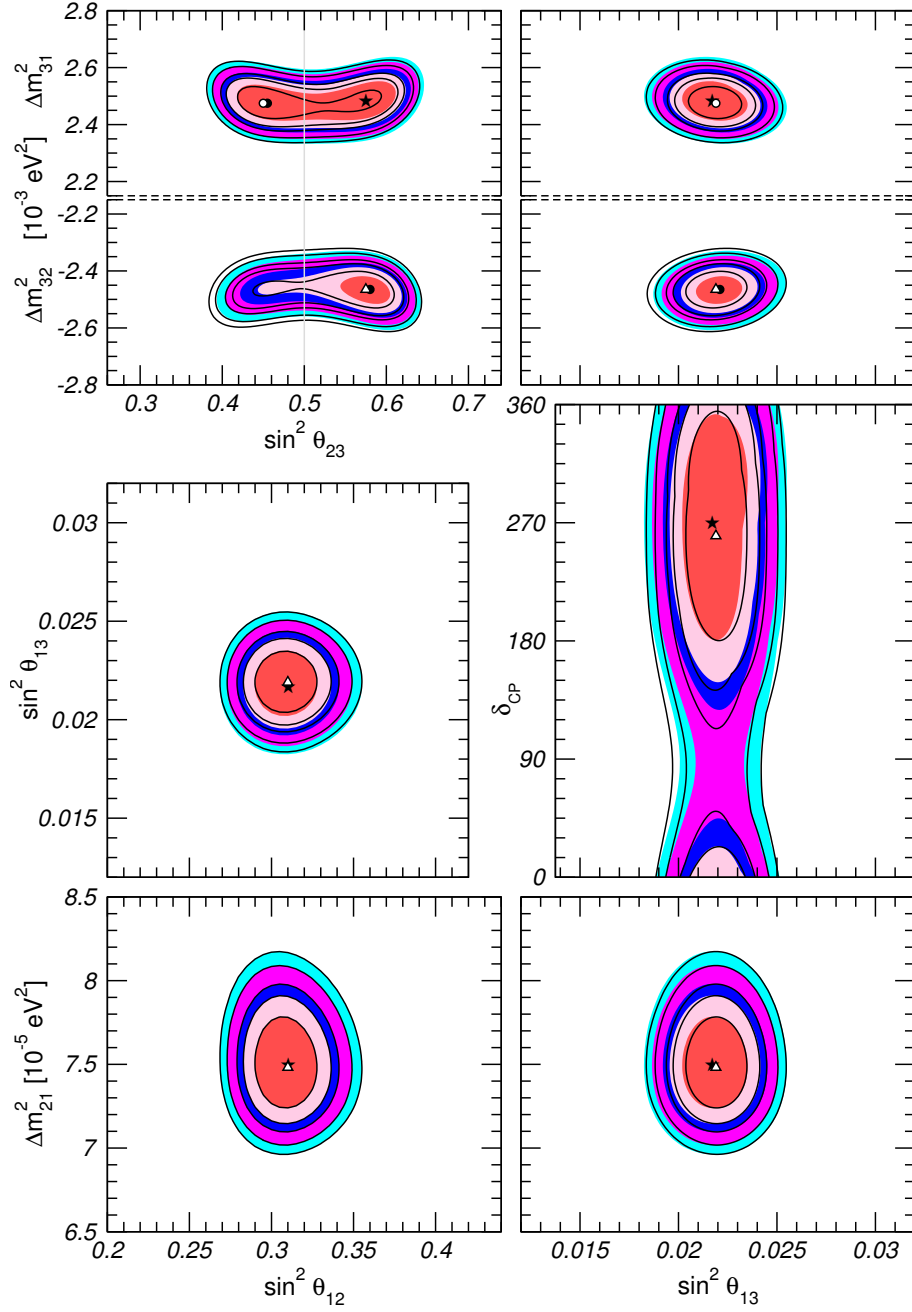


Fig. 2.9 Global 3-neutrino oscillation analysis taken from [70, 71]. Each panel shows the two-dimensional projection of the allowed six-dimensional region after marginalization with respect to the undisplayed parameters. The different contours correspond to 1σ , 90%, 2σ , 99%, 3σ CL (2 dof).

Table 2.1 The current best-fit values for the neutrino oscillation parameters for normal (inverted) hierarchy. Taken from [71].

Parameter	Best fit ($\pm 1\sigma$)
$\sin^2 \theta_{12}$	0.306 ± 0.012
$\sin^2 \theta_{23}$	$0.441^{+0.027}_{-0.021}$ ($0.587^{+0.020}_{-0.024}$)
$\sin^2 \theta_{13}$	0.02166 ± 0.00075 (0.02179 ± 0.00076)
Δm_{12}^2 [10^{-5} eV ²]	$+7.50^{+0.19}_{-0.17}$
$ \Delta m_{3\nu}^2 $ [10^{-3} eV ²]	$2.524^{+0.039}_{-0.040}$ ($-2.514^{+0.038}_{-0.041}$)
δ_{CP} [$^\circ$]	261^{+51}_{-59} (277^{+40}_{-46})

such as Equations 2.30 and 2.31, would be zero if there was no mass splitting). Three active neutrino flavours gives rise to two independent mass splittings, Δm_{12}^2 and Δm_{32}^2 , as appear in the oscillation probabilities. Unfortunately, fitting to the oscillation results provides only a handle on the value of these splittings and not the signs, resulting in an ambiguity in the ordering of the mass states. This can be resolved in the solar sector by utilising the effect of the MSW resonance encountered by neutrinos in the Sun, allowing the sign of Δm_{12}^2 to be known (it must be positive as otherwise fewer oscillations, not more, will have been observed by SNO and the other solar neutrino experiments). This leaves two possible ‘hierarchies’, normal and inverted, which are possible given the experimental data. These mass splittings also do not offer any indication of an absolute mass scale for the neutrino mass states, this must be constrained using other methods and is currently undetermined. These uncertainties are illustrated in Figure 2.10.

DUNE will use the MSW effect present as neutrinos propagate through the Earth’s crust in order to resolve the hierarchy problem. It is essential that the hierarchy is resolved since the associated asymmetries between neutrinos and antineutrinos can mimic true CP-violation, which therefore cannot be measured accurately until the mass splittings are completely understood. Due to the large matter effects associated with its long baseline, the NOvA experiment is sensitive to the mass hierarchy and may be able to have a say before DUNE and Hyper-Kamiokande.

The absolute neutrino mass cannot be measured from oscillation experiments so other techniques have been developed. It is possible to use information from β -decay to get a handle on the mass scale; the $\bar{\nu}_e$ mass alters the spectrum of electrons near the end point so precision measurements can study this effect. The current best limits on the mass are from H³ β -decay experiments and yield $m_{\bar{\nu}_e} < 2.05$ eV at 95% C.L. [77, 78]. Cosmological analysis can also constrain the absolute neutrino mass by looking at the distribution of matter

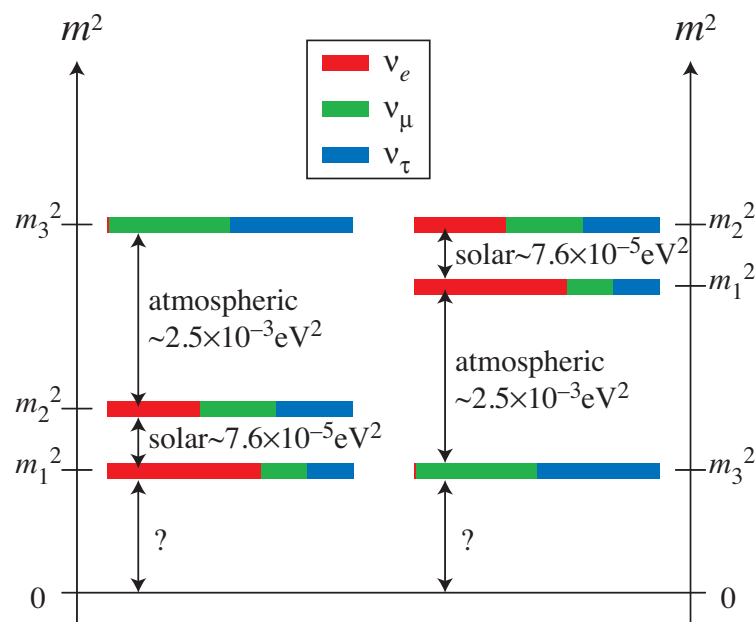


Fig. 2.10 Demonstration of the current uncertainties in the neutrino mass. The undetermined sign in the mass splitting between the 2 and 3 states leaves two possible ‘hierarchies’ open: normal (left figure) and inverted (right figure). The absolute scale of the masses is also currently unknown. The flavour composition of each of the mass states, given by the mixing angles, is denoted by the coloured bars.

in the Universe and information such as galaxy clustering. The Planck collaboration reported the upper limit on the sum of all neutrino masses as $\sum_i m_{\nu_i} < 0.23$ eV at 95% C.L. in 2013 [79], indicating a significantly lower mass scale than is attainable using current experiments.

2.4 The LAr TPC Concept

Lee: two things. Could this be in the DUNE chapter instead? I like it here I think, but would also work as an introduction to the next chapter. Also, this should be considered a VERY first draft! I imagine I will be coming back here often as I write and realise that I assumed something wrt LArTPCs which I had not already explained. Particularly in the last section, challenges.

The use of a liquid argon time projection chamber (LArTPC) as a high-precision fine-grained detector medium holds much promise for the successful resolution of the open questions in neutrino physics. A great amount of R&D work has taken place to advance the maturity of the technology and pioneering experiments, such as ICARUS [80], have further increased the understanding of the neutrino community of the detector techniques. Past and currently running experiments at Fermilab, such as ArgoNeuT [81], LArIAT [82] and MicroBooNE [83], are successfully using LArTPCs to take and analyse data and it seems certain to be the future of neutrino physics in the U.S. [84].

This section will provide a brief history of LArTPC technology and motivate its potential when used in a huge experiment such as DUNE. The basic operation of such a detector will also be described to provide background for discussion of the DUNE and 35 ton experiments, and of reconstruction in LArTPCs, in future chapters.

2.4.1 A Brief History of Time (Projection Chambers)

The use of a time projection chamber as a potential particle detector was put forward by David Nygren in 1974 [85]. He envisioned bubble-chamber quality data but with the possibility of digital readout of the data, facilitating extremely fine spatial resolution, good timing resolution and fast recovery after triggering. The basic concept is a drift chamber containing a noble gas placed within a field to drift ionisation electrons created by a propagating particle towards a multielectron array. This setup allows full three-dimensional reconstruction by combining information from the two-dimensional readout plane with the drift time. Nygren also included a magnetic field to assist particle identification in his design, shown in Fig. 2.11.

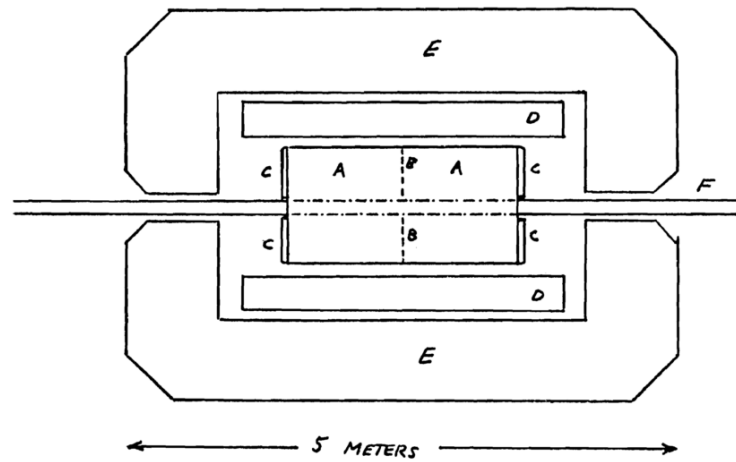


Fig. 2.11 The original concept of the time projection chamber particle detector, drawn by David Nygren in 1974 [85]. The sections are labelled as followed: methane-filled region (A), screen to establish electron field (B), end-cap detectors (C), superconducting solenoid (3.33 T) (D), iron return yoke for magnetic field (E), beam vacuum pipe (F).

The extension of this concept to a liquid argon TPC and its potential as a high-precision fine-grained detector medium in neutrino physics was proposed by Carlo Rubbia in 1977 [86]. The use of a noble liquid rather than gas is necessary in neutrino experiments to provide a high enough target mass for increased probability of neutrino interactions. Noble liquids have high electron mobility and low diffusion, favourable properties as the detection of particles is from the ionisation and scintillation light created by the particles. Given the necessity of a high electric field in order to drift these electrons to the readout places, excellent dielectric properties are also required; noble liquids possess such qualities. The properties of liquid argon which make it almost perfect for this use are demonstrated in the table in Table 2.2.

An additional advantage of this technology is the low threshold for detection; this is set by the ionisation threshold of liquid argon and is only 23.6 ± 0.5 eV [88]. Rubbia realised that a LArTPC could be the digital replacement for the high quality particle detection methods used in bubble chambers, very common in neutrino physics in the 1970s. He proposed the first LArTPC detector design, shown in Fig. 2.12, which bears a striking resemblance to the LArTPCs in use today.

Constructing and operating such a detector was beyond the technology of the time, and is still being understood today. The operation of a LArTPC detector and the challenges associated with this are the subject of Section 2.4.2.

Table 2.2 Properties of noble liquids relevant when considering a TPC medium for a neutrino experiment [87].

	Water	He	Ne	Ar	Kr	Xe
Boiling point [K] @ 1 atm	373	4.2	27.1	87.3	120.0	165.0
Density [g/cm^3]	1	0.125	1.2	1.4	2.4	3.0
Radiation length [cm]	36.1	755.2	24.0	14.0	4.9	2.8
Scintillation [γ/MeV]	-	19 000	30 000	40 000	25 000	42 000
dE/dx [MeV/cm]	1.9	0.24	1.4	2.1	3.0	3.8
Scintillation λ [nm]	-	80	78	128	150	175
Natural abundance (Earth atm) [ppm]	5×10^4	5.2	18.2	9340.0	1.10	0.09
Electron mobility [cm^2/Vs]	low	low	low	400	1200	2200

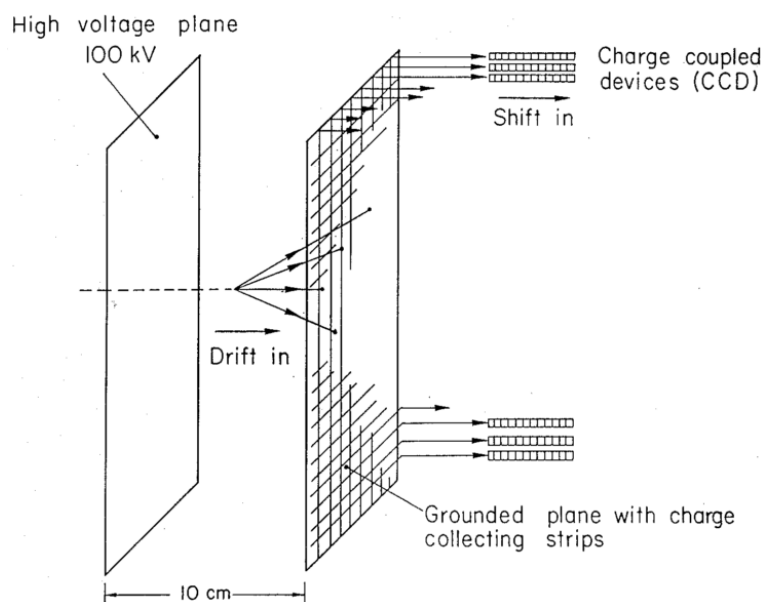


Fig. 2.12 The LArTPC detector proposed by Carlo Rubbia in 1977 [86].

2.4.2 LAr TPC Operation

A LArTPC typically consists of one or more anodes and cathodes at either end of an active drift region. An ionising particle passing through a LArTPC causes electrons to become free from argon atoms and, in the presence of a field, drift towards an anode where they are read out.

The readout consists of multiple wires planes with different orientations to facilitate the reconstruction. The wires are either ‘induction’ wires, which allow the electrons to deposit charge but continue past, or ‘collection’ wires, on which the electric field lines end and all the charge on the electron is collected. Each wire plane is therefore held at a different ‘bias voltage’ to prevent any field lines ending on the induction wire, thus creating local electric fields which promote the continuing forward motion of the electrons. The signal seen is therefore dependent on the type of wire plane; a bipolar pulse on an induction plane wire and unipolar on a collection plane wire. It is also common, though not essential, to make use of a ‘grid plane’ upstream of the signal planes in order to shield them from the electron charge until they are close. Without such a plane, the bipolar pulse would be highly asymmetric, though would still have zero integral. It also makes changing the drift voltage (controlling the electric field) slightly easier as the signal planes are somewhat shielded from its effects. MicroBooNE does not operate with a grid plane and, although the 35 ton and the DUNE reference design make use of a grid plane, it is uncertain whether the benefit outweighs the cost for a huge LArTPC detector such as the DUNE far detector. There are alternative readout possibilities to this typical design which have been suggested but, given the scale of future LArTPCs, it is highly unlikely a viable solution which delivers superior readout at a comparable cost will be found.

Upon ionisation, an electron has a certain probability (around 60%) of recombining before the field can separate it from its ion. Whilst this compromises the signal observed, it is accompanied by a flash of scintillation light which may be detected and used to assign an ‘event time’ to the interaction, known as T_0 . Without this information, it would be impossible to place an absolute time scale on the event and result in an unresolved coordinate along the drift direction. The magnitude of the applied electric field must be chosen to balance these two effects; a larger field would result in less recombination and therefore compromise the scintillation light while a smaller field would have consequences on the signal received at the wire planes. Figure 2.13 demonstrates this and justifies the field value of 500 V/cm which is often chosen in current LAr neutrino experiments.

The basic operational principles of a LArTPC is demonstrated in Figure 2.14. The specifics of how the ionisation charge and the scintillation light is collection and processed is experiment-specific and will be discussed in the context of DUNE in Chapter 3 and the

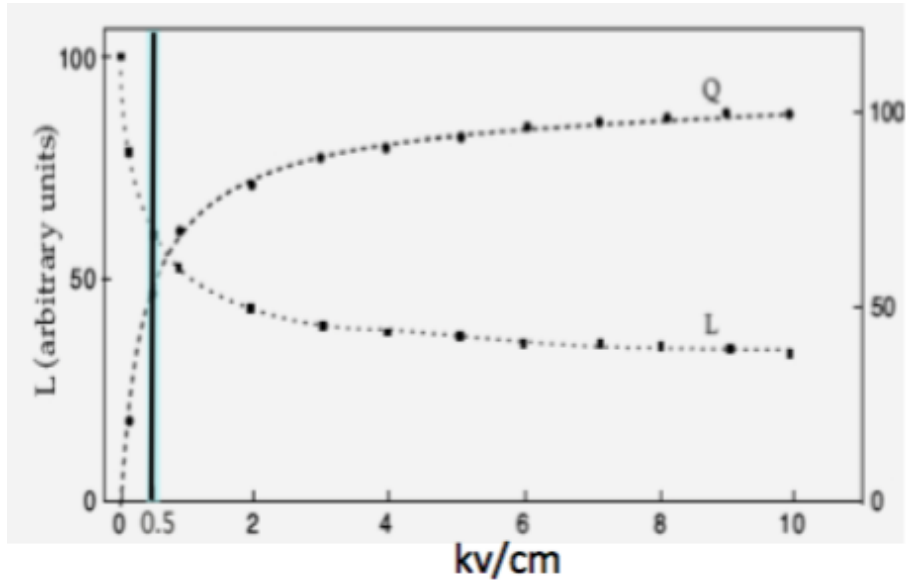


Fig. 2.13 Demonstration of the competing effect the electric field has on the luminosity of the ionisation electrons and scintillation light arriving at the detector readout. Since both are essential in reconstructing the complete interactions, a balance must be found. [PLACEHOLDER IMAGE].

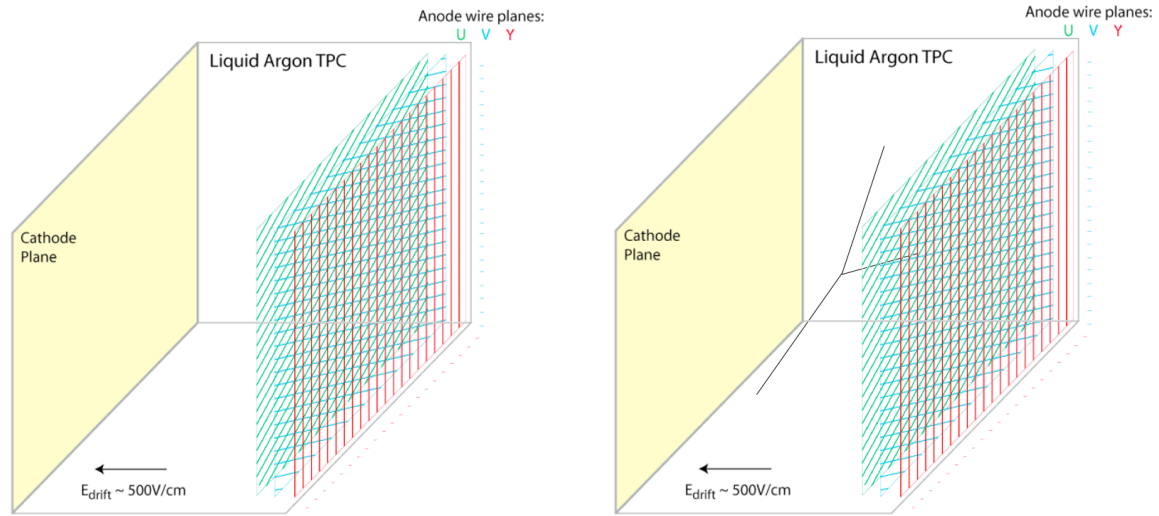
35 ton experiment in Chapter 4. This information is all that is required to fully understand and analyse the interactions occurring in the detector; methods used to reconstruct particles and interactions in LAr will be the subject of Chapter 5.

2.4.3 LArTPC Challenges

There is no doubt of the promise of LArTPCs for the future of neutrino physics but with such expectation comes many challenges. This will be elaborated upon in more detail when discussing the 35 ton run in Section 4.8 but will be briefly mentioned here for completeness.

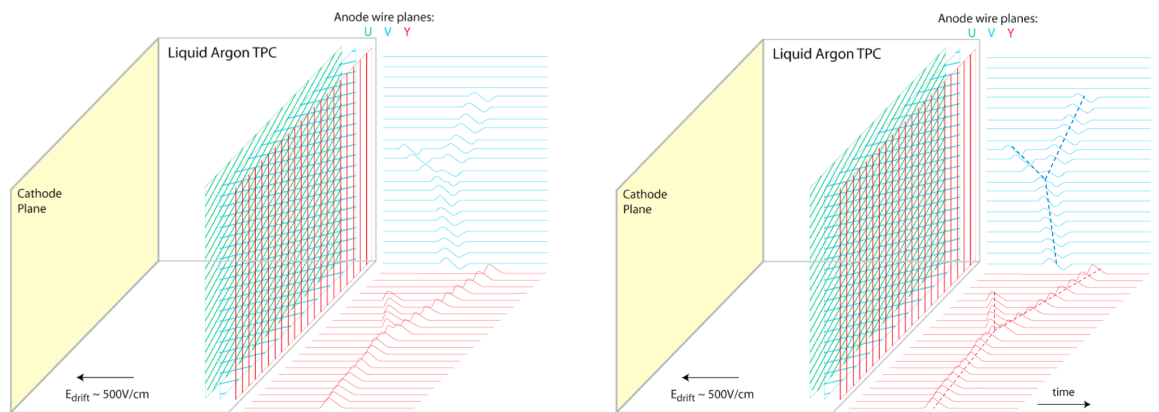
Given the drift fields required, and the necessary distances, the associated high voltage on the cathode must be on the order of ~ 100 kV. This presents engineering challenges related to feedthroughs and cryostat design but also can lead to dielectric breakdown of the liquid nearby such huge voltages. The properties of LAr and the design implications must be very well understood to ensure this does not endanger the quality of the detector medium.

The presence of electro-negative impurities in the argon can capture drift electrons as they travel towards the anode planes and hinder the signal observed. The probability of this recombination is referred to as the ‘electron lifetime’ and is directly affected by the maintained purity of the argon. DUNE expects a contaminant no greater than ## ppm O₂ and ## ppm N₂. This necessitates a purification system to remove impurities and requires



(a) Typical LArTPC with one cathode (left) and three read out anode planes (right) (two induction, U and V, and one collection, Y), setting up an electric field. The central region is filled with liquid argon.

(b) An ionising particle enters the detector and liberates electrons from the medium, which then drift towards the anode planes.



(c) As the electrons drift through, charged is induced on the first two wire planes and collected on the final one. Due to the differing orientations of the wires between planes, three complementary views of the interaction are provided (two are shown).

(d) By combining the two dimensional information provided by the anode planes with the drift time information, the original particle tracks can be inferred.

Fig. 2.14 Schematic demonstrating the basic operational principles of a LArTPC. The images are stills taken from an illustration created by Bo Yu (BNL) (do I need to cite this? It's a very common slide and I can't actually find a Bo Yu talk with it in... everyone just puts his name on the slide!).

the constant recirculation of the liquid through it. A liquifier is also necessary to recondense any boiled-off gases at the surface.

Along with the possibility of lost signal through finite electron lifetimes, the drift electrons may also undergo interactions and drift off course either transversely or longitudinally. This ‘diffusion’ affects the location and size of the observed signal so also must be well understood.

With so much resting on the success of the DUNE experiment, and considering all these effects which must be understood, prototyping is essential. The 35 ton prototype was constructed to attempt to better understand LArTPCs and is the subject of Chapter 4.

Chapter 7

Analysis of 35 ton Data

The 35 ton run (see Section 4) provided 22 days of good quality (high purity, stable field (250 V/cm), stable DAQ), analysable data. Due to the issues encountered, high quality physics analyses proved very challenging and instead more time was taken developing software to mitigate issues such as coherent noise and digitiser stuck bits. Analyses, particularly those presented here, focused on trying to understand the detector and characterise previously untested responses. In this respect, the 35 ton proves to be a vital experiment in informing the next generation of prototypes and even the final DUNE far detector design. It also boasts datasets which no planned experiment will before the full DUNE modules; it is therefore essential as much information as possible is extracted from the 35 ton analyses.

Before analyses are presented, techniques developed to enhance the quality of the data, and the data selection, will be discussed in Section 7.1. A short section demonstrating how LAr purity may be determined from data is contained in Section 7.2 before the main analyses, concerning tracks passing through the APA frames and across APA gaps, are presented in Section 7.3 and Section 7.4 respectively. Finally, a brief investigation into the performance of basic shower and calorimetric reconstruction on the 35 ton data is discussed in Section 7.5.

7.1 Preparing 35 ton Data for Analysis

To ensure analyses are as accurate as possible, careful pre-selection and preprocessing of the data is performed. Methods for producing the analysable sample are discussed in the section.

7.1.1 Selecting the Data

The level of noise present in the TPC data varied hugely between runs – this is evident from analysing the RMS of the charge read out on a particular channel. Figure 7.1 shows a comparison of this metric for ‘good’ and ‘bad’ runs.

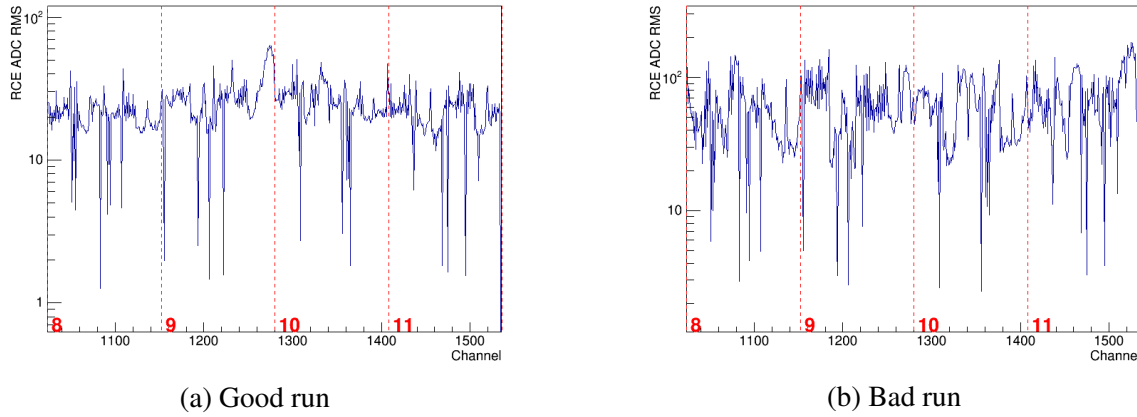


Fig. 7.1 Comparison between noise levels for ‘good’ and ‘bad’ 35 ton runs. The channels shown are on APA2 (online convention, APA0 offline) and are read out by RCEs 8 through 11 (labelled). The increase in read out charge RMS is evident in the case of the noisy run. These plots are from runs 15797 (Fig 7.1a) and 15790 (Figure 7.1b) and were taken only 50 minutes apart.

Runs which exhibited the lowest noise were selected for analysis. In all there were 1269 runs used representing some data taken before the FNAL site wide power outage (3rd March 2016) with most the week after stabilising the experiment again (9th March – 17th March). A selection of bad channels, classified as either ‘dead’ (electrically) or ‘bad’ (exhibit sufficiently more than average noise), represent 8% of the total number of channels.

Due to the continuous nature of data taking, there is a non-trivial correlation between a ‘DAQ event’, a collection of fragments read out by the DAQ, and a ‘physics event’, an event in which particle interactions occurred. The external triggers used in the 35 ton, namely the external muon scintillators and the photon detectors, are used to define the event time. Given the trigger rate at which most data was taken (~ 1 Hz), a typical run comprising a few thousand events will only contain $\mathcal{O}(10)$ triggered events. Furthermore, given the data format, these events often straddle multiple DAQ events (refer to Figure 6.5 for a demonstration of this). A splitter/stitcher module is employed to search for triggers within runs and construct physics events containing the useful information for analysis. This produces a file with just this relevant information, which are then used for analysis.

7.1.2 Improving Data Quality

Two issues present in the raw data, namely the presence of correlated noise and the stuck bits in the digitiser, are dealt with as an initial step of the reconstruction. First, an algorithm attempting to correct for the stuck bits analyses waveforms on a wire and identifies problematic ADCs; interpolating between charges read out at neighbouring times is successful at reconstructing the initial waveform in most cases. Figure 7.2 demonstrates this interpolation method on simulated data.

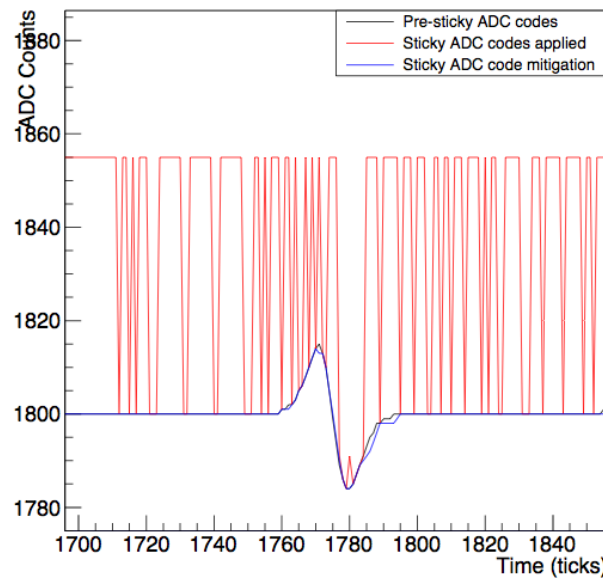


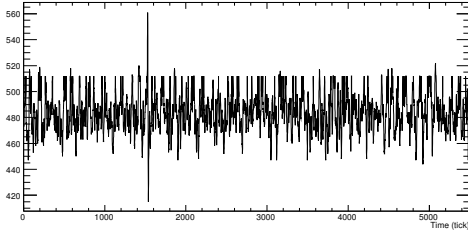
Fig. 7.2 Simulated demonstration of the method used to correct for stuck codes in the 35 ton data. On a given channel, ADCs exhibiting the consequences of this problem are corrected by interpolating charge at neighbouring time units. This is tested by simulating a waveform and adding the observed stuck code effect; the efficacy of the method at correcting the afflicted bits can then be evaluated.

The effect of applying this algorithm on a full waveform, to correct for all the stuck bits, is apparent in Figure 7.3.

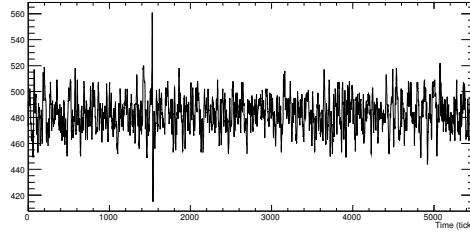
Following this process, a coherent noise removal stage is applied. This simply looks at the average noise across channels sharing a front-end voltage regulator and removes this component from the readout ADC for each channel. The effect of this correction is seen in Figure 7.4.

7.1.3 Reconstructing Muon Tracks

All analyses discussed below only make use of information recorded on the collection planes. Since the induction wires are longer (a necessity for wrapping), a larger capacitance

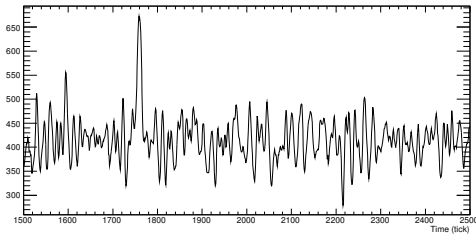


(a) Raw waveform before correcting for stuck bits.

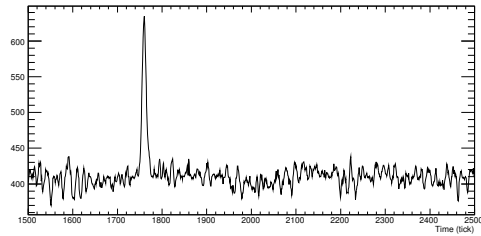


(b) After applying stuck bit mitigation.

Fig. 7.3 The effect of applying stuck bit mitigation to a waveform as seen in raw data. This particular waveform is from run 15660, channel 722 (induction channel).



(a) Waveform before removing coherent noise.



(b) After removing coherent noise.

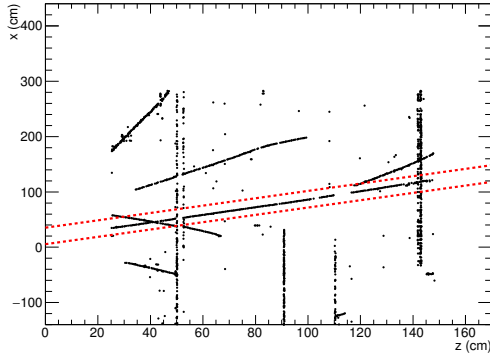
Fig. 7.4 The effect of removing coherent noise from all channels on a voltage regulator. This waveform is from run 15660, channel 2010 (collection channel). The signal is noticeably larger following this process, considerably improving reconstruction performance.

results in higher noise levels, complicating the reconstruction. In general, after applying the refinements outlined in Section 7.1.2, the signals on the collection channels are prominent enough for competent analyses. The methods used to select tracks are described in this section and applied during the subsequent studies.

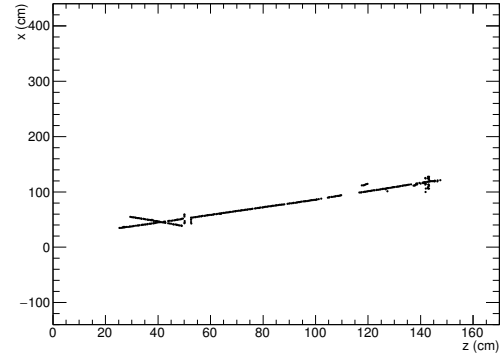
Using only the collection plane presents challenges, the most obvious being the impossibility of full 3D reconstruction. A hit on a collection wire at a given time gives well-defined x and z coordinates but cannot give any information in the y -direction. ‘Quasi-3D’ reconstruction is achieved by making use of the external counters. Through-going muons are triggered by the coincidence of hits in two opposite counters; this information can be used to give a crude handle on the y position of hits.

Figure 7.5 outlines the stages of selecting hits originating from the particle track which caused the trigger. Figure 7.5a shows all hits from an example event containing a through-going muon. The first stage of track selection involves taking those hits which lie in the ‘counter shadow’, the narrow section of collection plane area physically inbetween the opposing counters through which the triggering particle passed. The hits which remain are

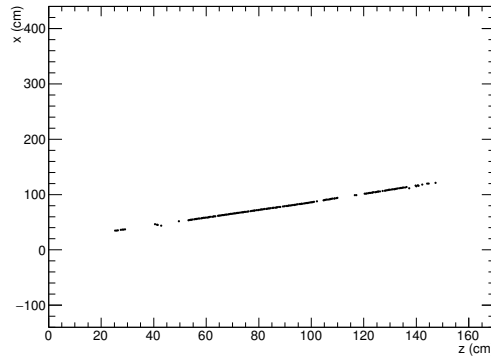
shown in Figure 7.5b. The track hits are visible along with further, unrelated hits. These are removed by requiring that only hits on wires with single occupancy be kept, and then applying a linear fit and removing all hits with residual > 2 cm. The final output after these stages is shown in Figure 7.5c.



(a) All hits before any track selection. The red lines represent the boundary defined by the edges of the two counters causing the trigger.



(b) Hits in the counter shadow.



(c) Hits on single wire occupancy and with residual < 2 cm.

Fig. 7.5 Demonstration of the successive stages applied to hits on collection wires in order to select hits from the through-going track associated with the particle which caused the trigger. The hits left after all stages are taken forward into the analyses.

The result of this track selection, as evident from Figure 7.5c, is a well-formed, high quality track with which it is possible to perform analyses. These will be the focus of the remainder of this chapter.

7.2 Measuring LAr Purity from Crossing Muons

7.3 APA-Crossing Muons

The 35 ton is the only proposed experiment before the full DUNE far detector modules that have fully implemented anode planes within the cryostat reading out data from multiple drift regions simultaneously (ProtoDUNE will have wrapped wire APAs but will only read out one drift region each and SBND has the CPAs in the centre of the cryostat with the APAs at the edges). Referring to Figure ??, this is a design consideration that features prominently in the eventual detector so any implications in the data must be well understood. Analysis of tracks which pass through the APAs and deposit charge in both drift regions is the subject of this section.

In Section 7.3.1, a method to determine the absolute event time, T_0 , from APA crossing tracks is presented and in Section 7.3.2 the charge deposited by these tracks, particularly when crossing through the planes, is studied. Comparisons between the two drift regions, made possible by comparing tracks left by the same particle, are contained in Section 7.3.3.

7.3.1 T_0 Determination from APA Crossing Tracks

Given the nature of a TPC detector, an ‘event time’ (T_0) must be known in order to set an absolute timescale, and therefore absolute position, on all interactions within the detector. An accurate T_0 is essential for calorimetric reconstruction: in order to understand how much charge a hit had when it was created, a lifetime correction dependent on the total drift time must be applied. An incorrect T_0 would lead to a systematic under- or over-estimation of the reconstructed energy and have implications in particle identification and shower energy determination.

In a LArTPC, an event time is usually given by an external triggering system. The DUNE far detector will rely on the instantaneous detection of photons produced from the immediate recombination of the ionisation electrons with positive Ar ions. In the 35 ton, an additional external system was provided by the scintillation counters. Since the sample of APA crossing muons used in this analysis were all selected and reconstructed using counter information, an interaction time is immediately known.

Without correctly accounting for T_0 , the tracks on each side of the APAs appear offset from the planes. This is evident from the event display shown in Figure 7.6. By aligning the track segments on either side of the APAs, a measurement of T_0 can be made directly from the TPC data.

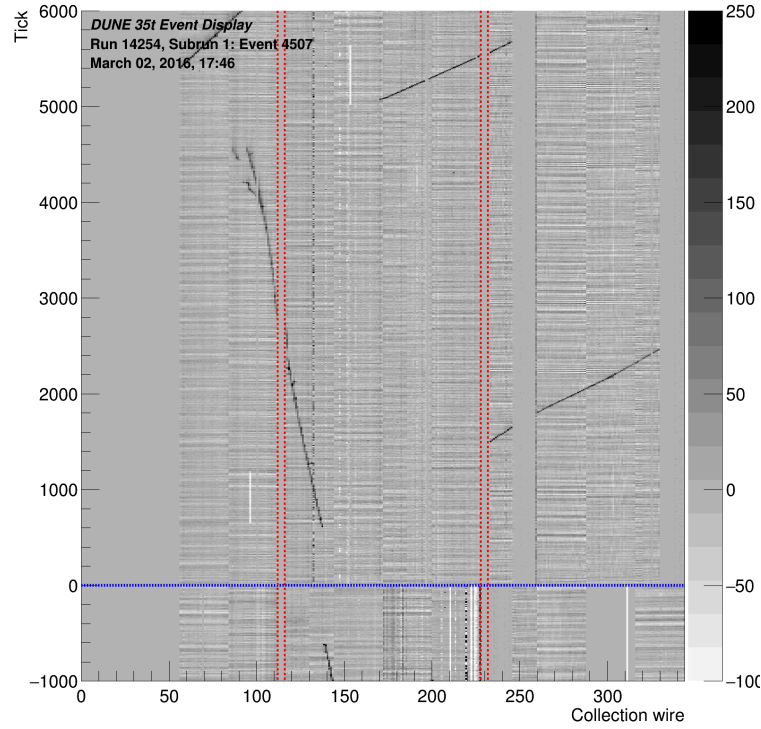
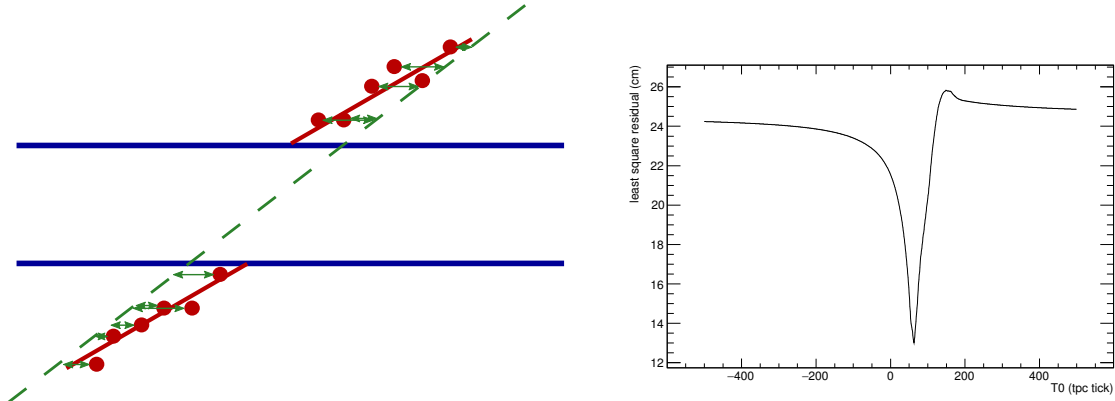


Fig. 7.6 Event display made during the run in which a track passes through the APAs. Correcting for T_0 would eliminate the visible offset and result in a single accurately connected track.

7.3.1.1 Aligning APA Crossing Tracks

Two complementary methods were used to accurately align the track segments across the APA. Both involved initially correcting for the counter T_0 , T_0^{counter} , before considering a range of alternative T_0 hypotheses and minimising a relevant metric to determine the most likely value. In the first method, demonstrated in Figure 7.7, a least square linear fit is applied to the track and the residual minimised. The second method, demonstrated in Figure 7.8, involves fitting a line to each segment in turn and minimising the projected distance between the intersections of the lines with the centre of the APAs ($x = 0$). As will be shown later, and can be seen from Figs. 7.7b and 7.8b, the two methods agree very well with each other.

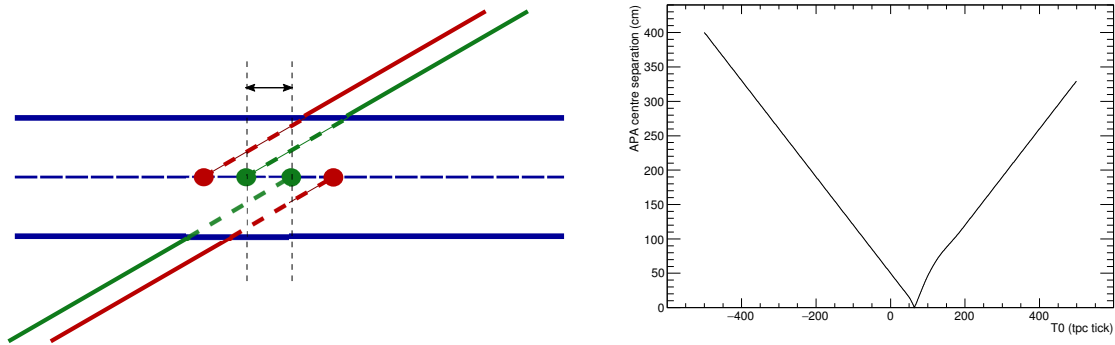
Naively, one would expect the T_0 determined using these methods, T_0^{TPC} , to agree with T_0^{counter} . It was noted however that there appeared to be a systematic offset between the T_0 given by the counters and measured from the TPC data. The distribution of this disparity is shown in Figure 7.9; it peaks very sharply around 64 ticks ($32 \mu\text{s}$) and is importantly inconsistent with zero. This suggests an inconsistency somewhere in the data taking and will be the subject of the remainder of this section. Figure 7.10 shows an example track before and after this disparity is corrected for.



(a) Demonstration of the calculation of residuals from a linear fit through all hits. The red points are hits and the green line represents a linear fit through all points on both sides of the APA.

(b) The residuals to the linear fit of the track over a range of T0 candidates. The value of T0 which minimises this distribution (62 ticks in this case) is considered the most likely interaction time.

Fig. 7.7 Method to align track segments on either side of the APAs involving minimising residuals from a linear least square fit. A fit is applied to all hits and the resulting residual, a representation of the 'goodness of fit', is minimised over a range of T0 candidates to find the most likely interaction time for the particle leaving the track.



(a) Demonstration of the determination of the distance between the track segments at the centre of the APAs. The red and green lines represent linear fits to the hits (applied separately on each side of the APA) for different values of T0.

(b) The separation distance over a range of T0 candidates. The value of T0 which minimises this distribution (63 ticks in this case) is considered the most likely interaction time.

Fig. 7.8 Method to align track segments on either side of the APAs involving minimising the distance between the projected intersection of each with the centre of the APAs. A fit is applied to each track segment separately and the distance between the intersection of these lines with the centre of the APA is minimised over a range of T0 candidates to find the most likely interaction time for the particle leaving the track.

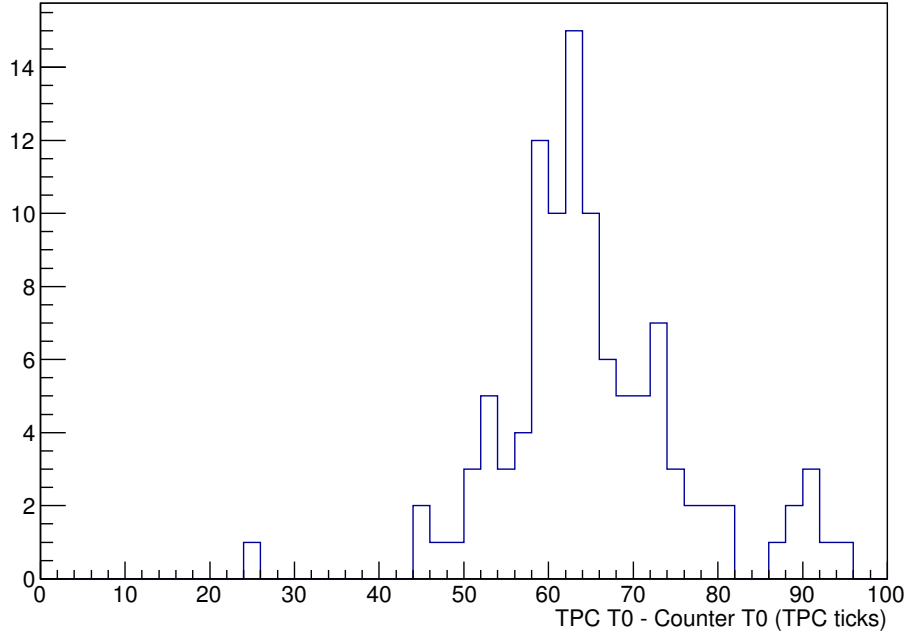
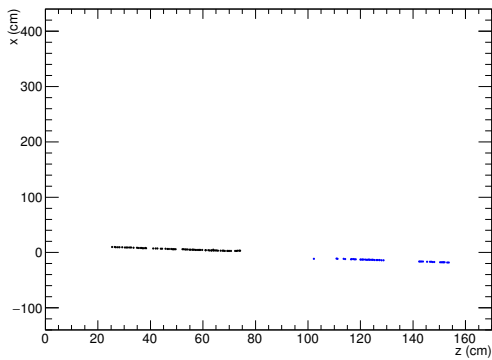
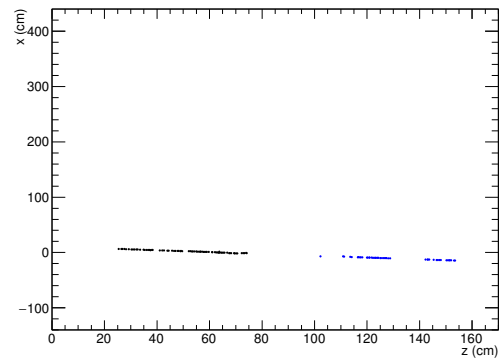


Fig. 7.9 [Placeholder image until I get one with full stats again!] Difference between the T0 calculated from TPC data and the T0 provided by the counters representing the trigger time of the through-going muon. If the two measurements of T0 agreed the distribution would peak at zero; the fact it does not is indicative of a systematic offset somewhere in the data taking.



(a) Correcting for T_0^{counter} .



(b) Correcting for T_0^{TPC} .

Fig. 7.10 Correcting for T0 using T_0^{counter} (Figure 7.10a) and T_0^{TPC} (Figure 7.10b). The difference is subtle but obvious; the method for determining T0 directly from the TPC data can be validated by eye. The minimisation of the metrics to determine T_0^{TPC} in this case are demonstrated in Figs. 7.7b and 7.8b.

Attempts to understand the misalignment of the tracks across the APAs are presented in the remainder of this section.

7.3.1.2 Understanding the Misalignment of APA Crossing Tracks

The underlying issue described above is essentially a misalignment of the same particle track between the two drift regions (see Figure 7.11). This obviously is not physical and stems from an issue with the detector or data readout. The most obvious cause is a miscalibration of the DAQ timing systems for the separate detector components, as previously assumed; there are however other possible causes for this problem. Most likely, the effect arises from a combination of these different factors.

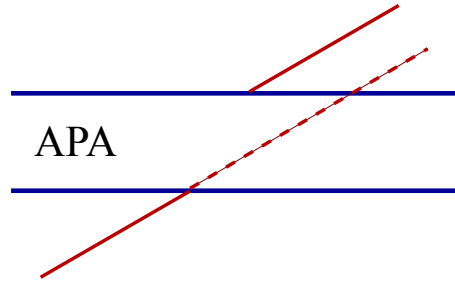


Fig. 7.11 (Possibly unnecessary, but helps to explain all the various factors which could explain the offset. Can remake if necessary.) Demonstration of the effect observed in the 35 ton data concerning tracks crossing the APAs. Even after correcting for the T0 provided by the counters, there is still a misalignment of the track segments across the APA frames.

Geometry Apart from timing, a misunderstanding of the geometry could explain this perceived misalignment. The spacing between the collection planes is one such example, as demonstrated in Figure 7.12a; the spacing necessary to explain this effect, determined by aligning the tracks using the methods discussed above over a range of collection plane spacing hypotheses, is demonstrated in Figure 7.12b. As is evident from the figure, the collection planes must be repositioned in such a way that they would be reversed; the track alignment complications cannot be explained solely by this.

A further problem is related to the wire positioning on the APAs in the z -direction; it is understood there may be a discrepancy between the two sides of the APA resulting in hits from the long and short drift regions at the same z -position reconstructed with a systematic offset. Figure 7.13a shows how this could be utilised to explain the apparent track misalignment with Figure 7.13b showing the distribution of corrected z positions necessary to resolve the issue. Offsets of ~ 30 cm, as suggested by these results, are impossible, indicating again the track alignment problem cannot be resolved in this way.

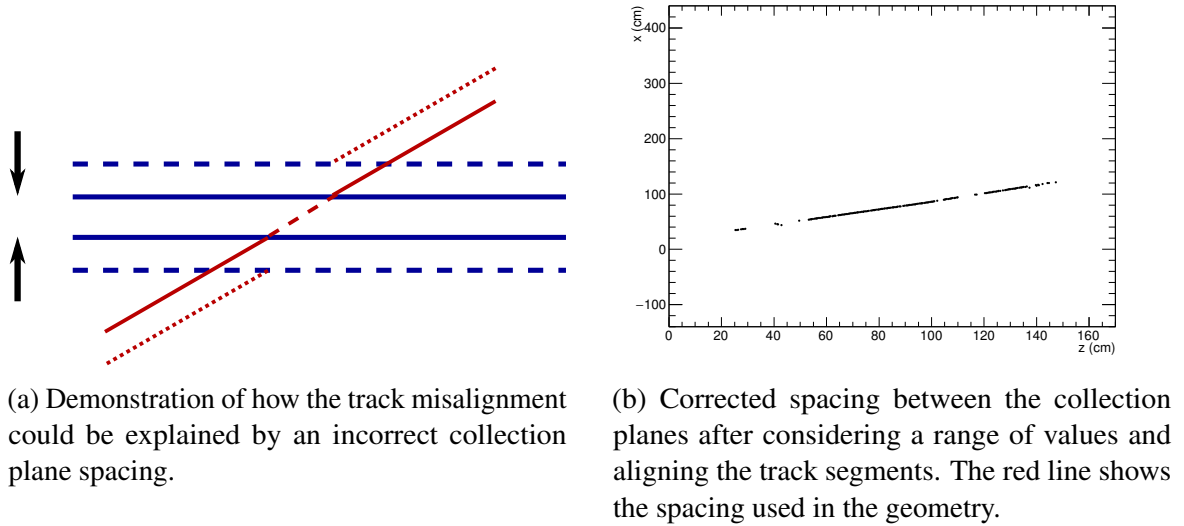


Fig. 7.12 Attempting to correct the track segment misalignment by assuming a misunderstanding of the spacing between the collection planes. It appears the resulting spacing necessary to correct for this issue would involve physically reversing the order of the planes.

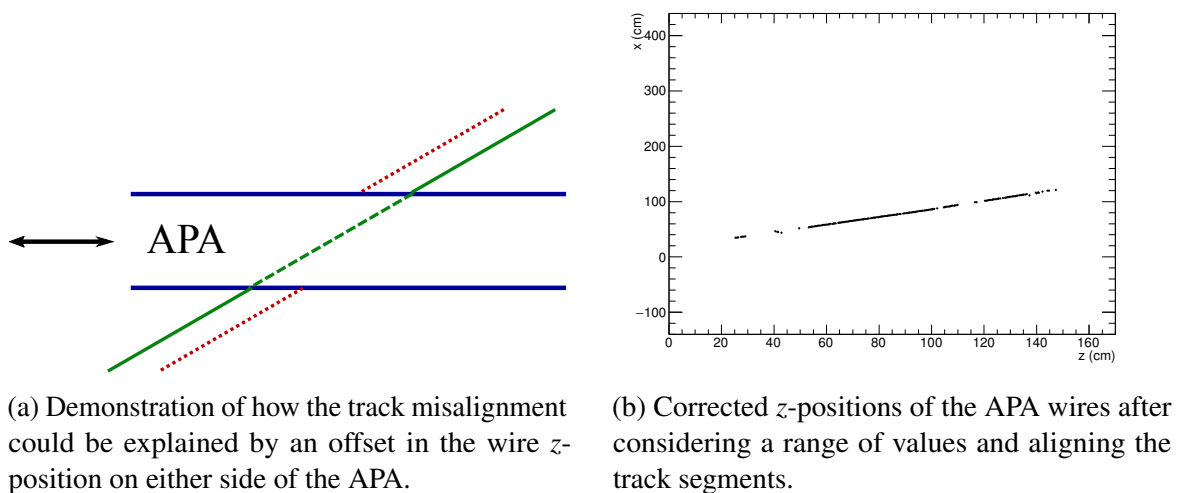
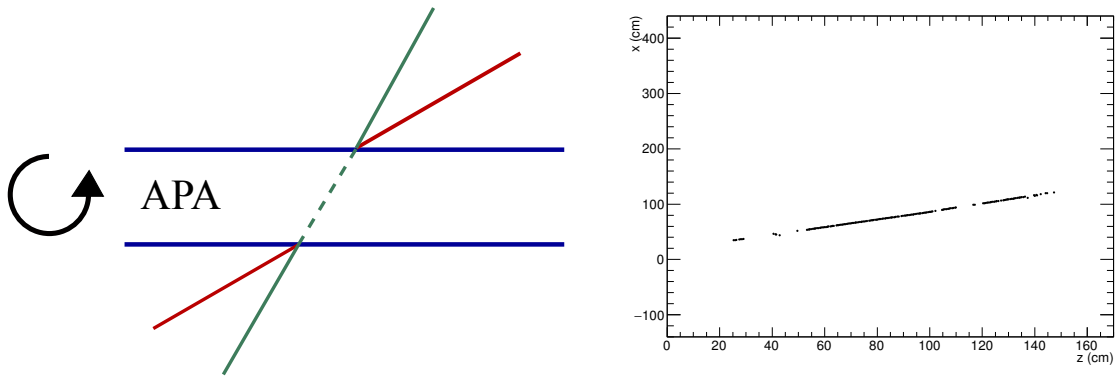


Fig. 7.13 Attempting to correct the track segment misalignment by assuming a misunderstanding of the positioning of the collection wires inside the detector. The wire offset would have to be around a foot to fix this issue.



(a) Demonstration of how the track misalignment could be explained by an incorrect drift velocity.

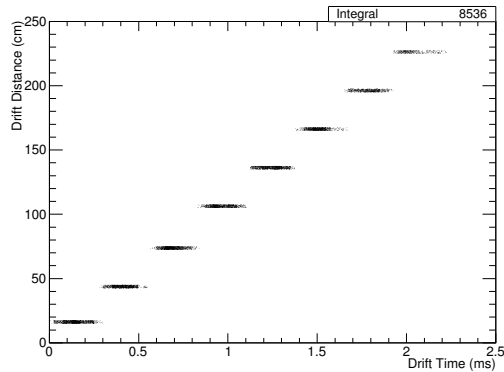
(b) Corrected drift velocity required to align the track across the APAs.

Fig. 7.14 Attempting to correct the track segment misalignment by assuming an incorrect drift velocity. In order to account for the effect noted in the data the drift velocity would have to around five times larger than that initially calculated from models.

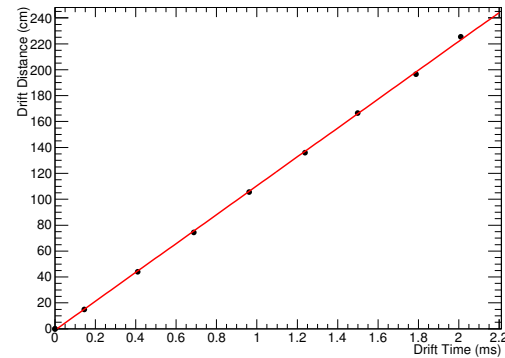
Drift velocity The drift velocity affects the angle of the tracks in wire/time space; a high velocity would result in a refraction-like effect towards the APA planes. As demonstrated in Figure 7.14a, this could explain the track segment misalignment if the effect was large enough. Figure 7.14b shows the necessary drift velocity required to account for the disparity observed in data; compared to a nominal value of 109 cm/ms, the scale of the change required to explain the oddity is unreasonably large.

This can be tested by measuring the drift velocity directly from the data. Taking tracks which pass through opposite counter pairs and comparing this drift distance with drift time is a trivial exercise, demonstrated in Figure. 7.15. The measured value of 110 cm/ms agrees exceptionally well with the aforementioned value, determined theoretically, of 109 cm/ms. It may therefore be assumed the drift velocity is as expected and does not contribute at all to the track alignment anomaly.

Timing The timing offset calculated in Section. 7.3.1.1, $32 \mu\text{s}$, is so large it was assumed another explanation for the track segment misalignment was likely. However, after reviewing all possibilities it appears there must be a significant timing offset present somewhere in the data. Further evidence for this hypothesis is presented in Figure 7.16 which displays the T0-corrected time distribution for all hits on the APA crossing track. The minimum drift time these hits may have, since they pass directly through the planes, is the interaction time, T0. As is evident from the distribution in Figure 7.16b, this is around 56 ticks ($28 \mu\text{s}$) and is



(a) Distribution of hit drift times for eight sets of counter pairs, assuming all tracks pass through the centres of the counters.



(b) The eight points found from taking the Gaussian mean of the time distributions for each rough drift distance.

Fig. 7.15 Measuring the drift velocity of the ionisation electrons by taking tracks passing through opposite counter pairs and comparing the corresponding drift distance to the drift time. Assuming all tracks pass through the geometric centres of the counters, a poor assumption, a distribution of hit time for this drift distance can be found; this is shown in 7.15a. Taking each counter pair separately and fitting a Gaussian to the distribution of drift times nullifies the assumptions necessary due to a lack of exact knowledge, on a track by track basis, of the exact x -position. This is shown in the graph in Figure 7.15b.

notably inconsistent with zero. The curious spike at the interaction time motivates the work presented in Section 7.3.2 and will be discussed there.

This interesting result provoked further investigation into the notion of a timing offset between detector components, specifically the TPC and counter readout (RCEs and PTB respectively). Confirmation of this miscalibration is displayed in Figure 7.17 which shows the difference between the timestamps recorded by each of the subcomponents upon receiving the trigger.

Within the limitations of all methods discussed, there is agreement between the T0 offset in Figure 7.16b and the timing miscalibration in Figure 7.17. This does not however account for the full track segment misalignment; this represents 64 ticks ($32 \mu\text{s}$) if accounted for using timing alone, as seen in Figure 7.9. As previously noted, the complete solution is likely a combination of different effects. Given that drift velocity and z -position of wires effects are negligible, the remaining offset must be due to a slight discrepancy between the actual spacing of the collection planes and what is being assumed. With an actual T0 of 56 ticks, this collection plane spacing can be determined in the usual way by aligning tracks. The results of this are demonstrated in Figure 7.18.

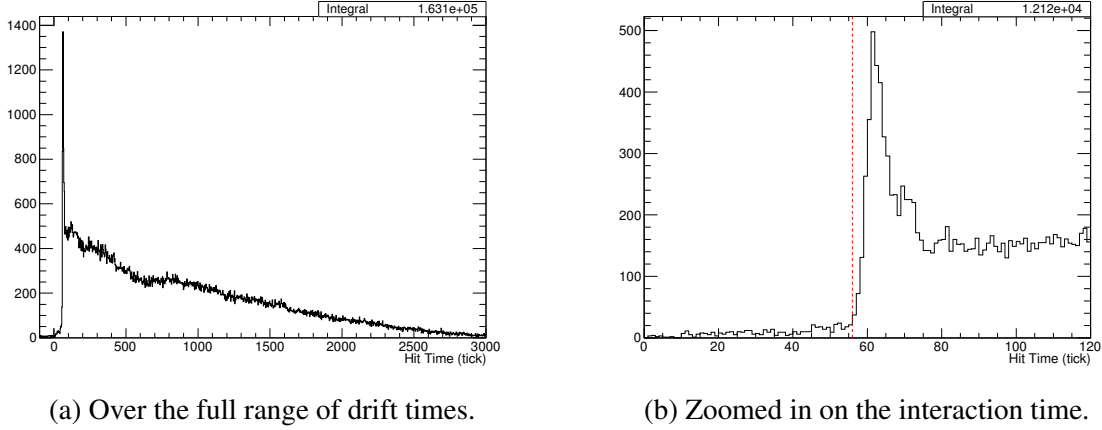


Fig. 7.16 The T0-corrected drift time for hits on APA crossing tracks. The lower leading edge of this distribution is an indication of the interaction time, T0. The red line on Figure 7.16b is drawn at 56 ticks ($28 \mu\text{s}$) and represents, by eye, the start of the distribution.

The misalignment of the tracks, as described in Section 7.3.1.1, can be understood as a combination of a timing miscalibration between two detector components and a slight offset in the geometry, which is not unexpected. This is the first time tracks crossing the readout planes have been used in a LArTPC experiment and have proven to be a valuable way of calibrating inter-detector components and finding other inconsistencies in the data. Without studying this data set, the timing offset between the TPC and the external counters would not have been discovered and all analyses would naively use the incorrect T0. In the next section, another source of information which can be gleaned from this dataset, this time more about understanding detector responses, will be discussed.

7.3.2 Charge Deposited by APA Crossing Tracks

The intriguing distribution of the T0-corrected hit times observed in the data, shown in Figure 7.16a, hints at some aspect of the detector response that needs to be understood. In the DUNE far detector, a large number of events will contain particles which pass through the APA frames so characterising resulting effects is critical. The equivalent plot for simulated data, filtered by those triggered using external counters and processed in the same way, is shown in Figure 7.19. Comparing these distributions, there is a very obvious difference around the interaction time. It appears there is an effect present in the data, not currently being simulated, which manifests in around twice the amount of hits occurring at T0 on the collection planes for APA crossing tracks. This is described in Section 7.3.2.1 and the phenomenon is visible on event displays presented in Section 7.3.2.2.

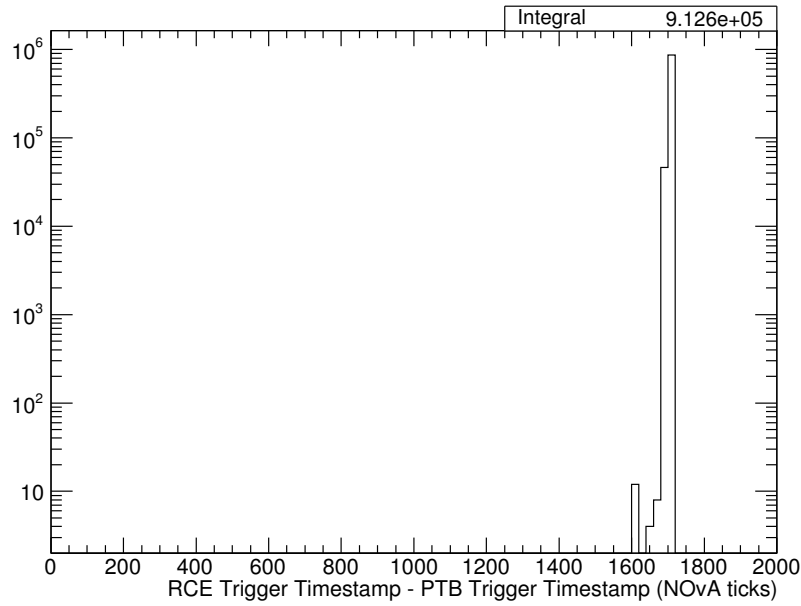


Fig. 7.17 The difference between the timestamps recorded by the PTB and the RCEs upon receiving a trigger. The absolute timing for the DAQ system is given, along with most experiments at FNAL, by ‘NOvA time’: a 64 MHz clock starting on 1st January, 2010 (with one NOvA tick therefore being 15.625 ns). The distribution peaks sharply at 1705 NOvA ticks, or 26.6 μ s.

Fig. 7.18

7.3.2.1 Interaction Time Hits

The excess of hits at the interaction time is due to the use of a grounded ‘mesh’ at the centre of the APAs. The purpose of such a design choice is to ensure a uniform electric field across the face of the APA; without it the field would be ill-defined given the presence of the grounded, rectangular APA frames with positively biased planes on either side. It is plausible therefore to consider a ‘backward-facing’ field being set up between the grounded mesh and the positively biased collection planes which would lead to hits drifting the ‘wrong’ way when produced in this region; APA crossing tracks would hence leave twice as many hits on the collection plane as the other planes. This is demonstrated schematically in Figure 7.20.

A convenient way of confirming whether or not the mesh can explain this excess of hits at the interaction time is possible since one of the four APAs in the 35 ton was constructed without the mesh, precisely for this purpose. Unfortunately, this was the APA which was more plagued by noise issues so very little good data is available from channels on this APAs. It is however possible to make a crude comparison; this is shown in Figure 7.21. The appears

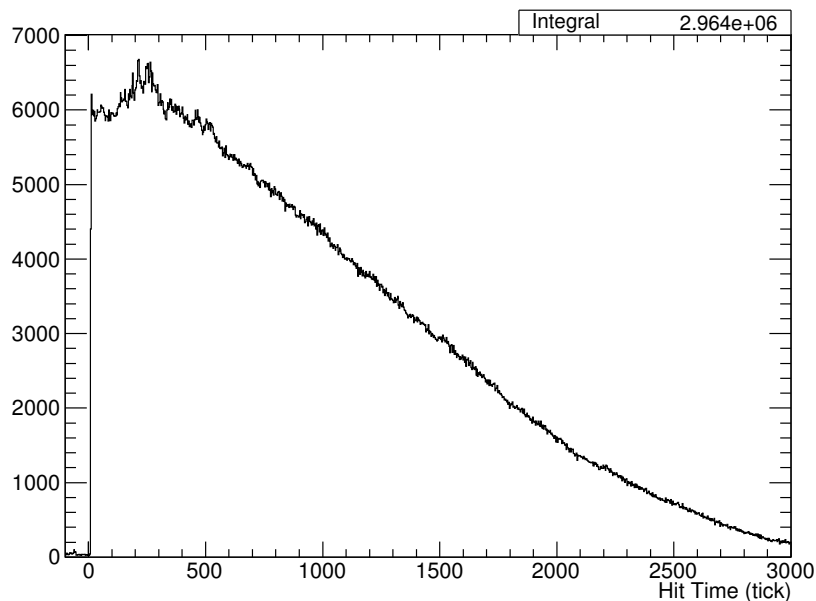


Fig. 7.19 The T0-corrected drift time for all hits on an APA crossing track in simulation. The equivalent plot for 35 ton data is shown in Figure 7.16a.

to confirm the shark peak of hits occurring at the interaction time comes from the APAs which use a mesh.

Using the 35 ton dataset, it is also possible to confirm that the mesh is functioning as expected. Without a mesh, one may expect a difference between the hits deposited on wires towards the centre of an APA face and wires at the edges, in front of the grounded frame. The functionality of the grounded mesh ensures there is no difference between any wires on a given APA. Figure 7.22 confirms this is the case.

A natural question to pose at this point is to ask if these ‘extra’ hits deposited by APA crossing tracks as a result of this ‘backwards’ field have similar properties to the ‘correct’ hits. The most important property to consider is the charge of the hits; Figure 7.23 shows the average charge per hit for hits occurring at the interaction time and all other hits. It is clear from this there is nothing different about these additional hits and they can be treated in the same way.

As alluded to earlier, the DUNE simulation software is simplistic and does not simulate any ionisations within the region of the APA planes; in the case of APA crossing muons this results in no hits being created after the track passes through the first induction wires. Evidently, this is an important region and must be understood and well simulated in order to test reconstruction and analyses. When this is added to the software, the 35 ton data will be essential for validation purposes.

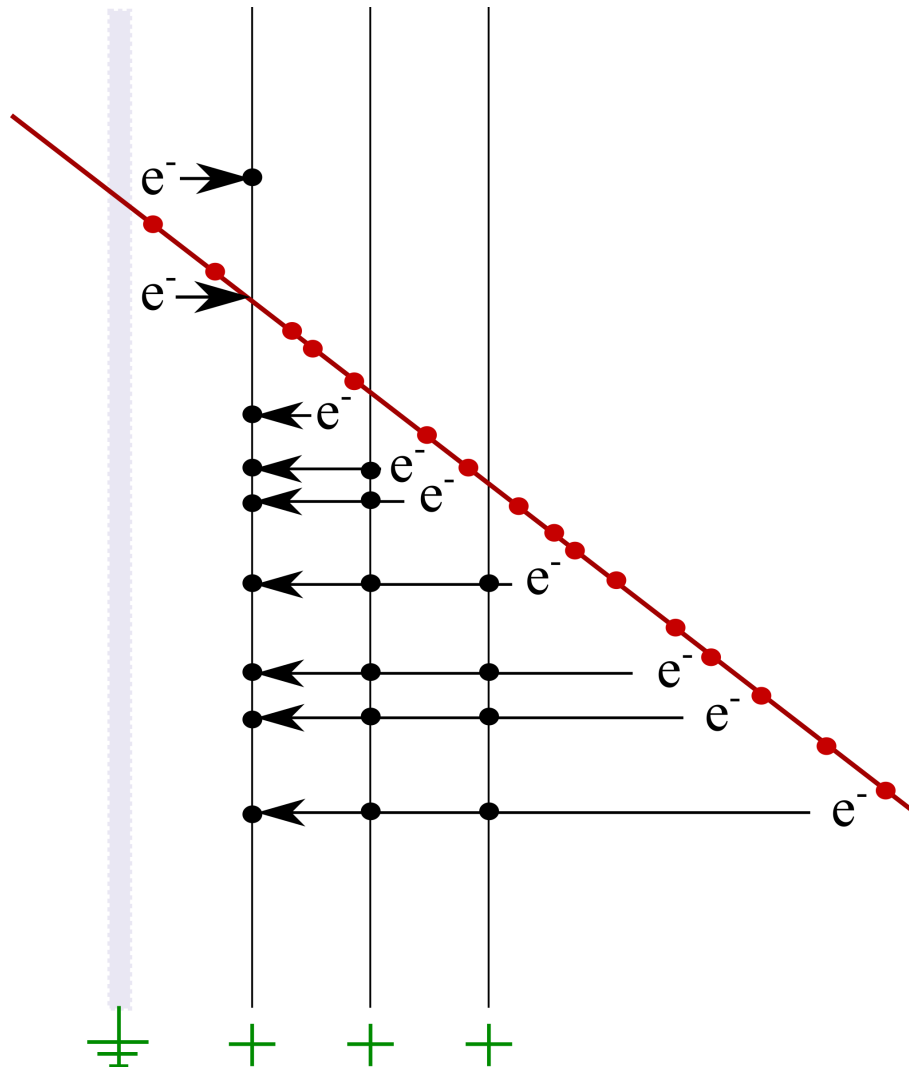
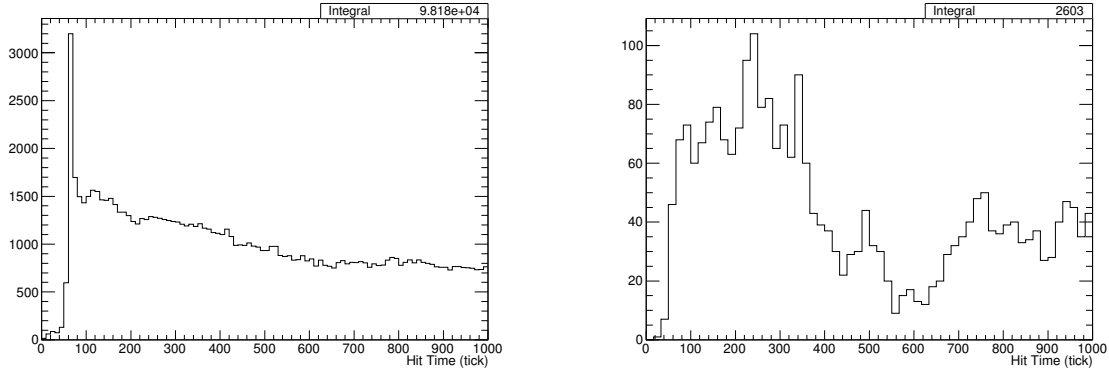


Fig. 7.20 Demonstration of the ionisation and hit collection for APA crossing tracks. The red line represents a track passing through the anode planes, shown in black. The grey region is the centre of the APA frame on which the grounded mesh is affixed. The red dots correspond to the ionisation of electrons which then drift, depositing charge (black dots) on the readout wires. The three planes shown are, from left to right, the collection plane and the two induction planes. The biasing of each of the planes and mesh sets up field lines which all terminate on the collection wires, resulting in charge collected from before the track passes through and after.



(a) Hit times for all hits on APAs 0, 2 and 3; these are the three APAs containing the grounded mesh at the centre.

(b) Hit times for all hits on APA 1, the APA without a grounded mesh at its centre.

Fig. 7.21 Comparison between the T0-corrected hit time distributions on APAs with and without the grounded mesh. Even given the very low stats in Figure 7.21b, there is a noticeable difference in the distribution of hits around the interaction time.

7.3.2.2 Event Displays of APA Crossing Tracks

The effect investigated in Section 7.3.2.1 is directly observable in the raw data, as shown in Figure ???. The electrons ionised as the particle track passes between the collection plane and the mesh are observable as hits which appear to have drifted in the negative time direction. The outcome is a little ‘hook’ shape in the data.

7.3.3 Comparison Between Drift Regions Using APA Crossing Tracks

APA crossing tracks may be utilised to make unique, specific measurements of the detector made possible since they originate from the same particle. For example, any drift velocity differences between the drift regions may be observed and the noise levels on the collection readouts on either side of the APA can be studied and compared.

The drift velocity is given by the angle of the track in wire/time space and any difference between this velocity in the two drift regions would be noticeable in a refraction-like effect. This is demonstrated in Figure 7.24a. A measure of the angle between the track segments in the different regions would therefore be a measure of the change in drift velocity; this is shown in Figure 7.24b.

The relative noise on the two collection planes can be evaluated by considering the number of hits present in the counter shadow, in each drift region, which were not reconstructed as part of the track associated with the triggering particle. The difference between each

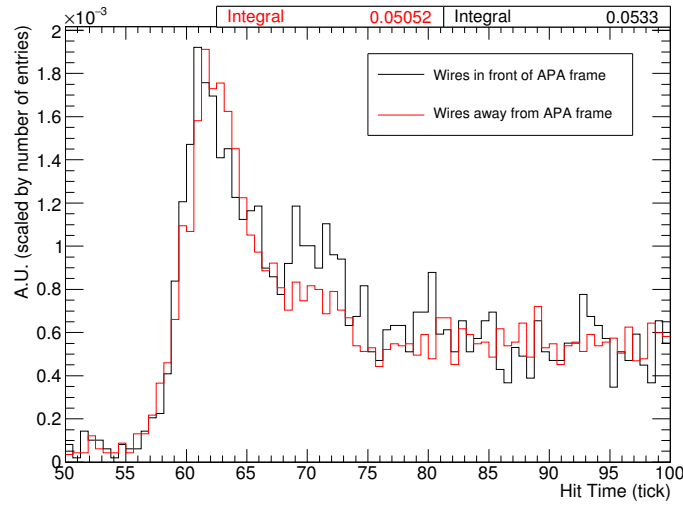
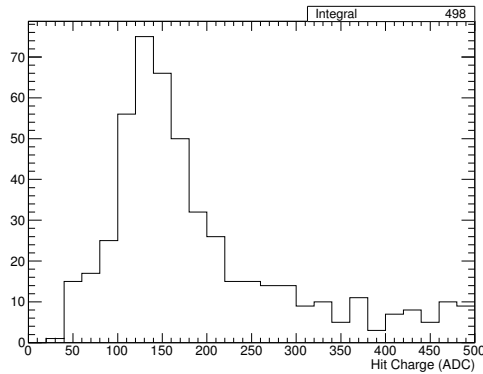
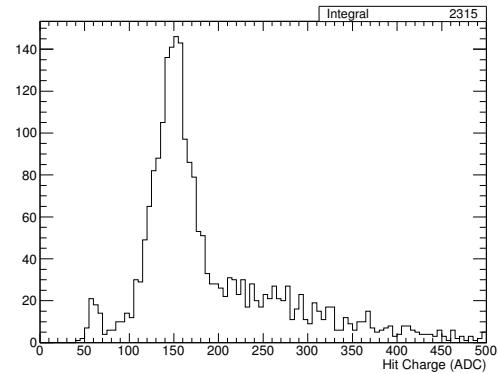


Fig. 7.22 Comparison between the distribution of T0-corrected hit times for hits on wires in front of the APA frame and away from the APA frame to validate the functionality of the mesh. Both distributions are normalised by the number of entries. There is no evidence of any differences between the two distributions so this suggests the mesh is working as intended.



(a) Hits occurring around the interaction time; $50 < \text{tick} < 70$. A fitted Gaussian of the peak yields a mean of 149 and width of 49.



(b) Hits occurring away from the interaction time; $\text{tick} < 50, \text{tick} > 70$. A fitted Gaussian of the peak yields a mean of 152 and a width of 28.

Fig. 7.23 Average lifetime-corrected charge per hit for hits on an APA crossing track separated according to whether or not the hit was collected around the interaction time. There is no evidence to suggest the ‘extra’ hits collected around the interaction time have significantly more or less average charge than ‘regular’ hits.

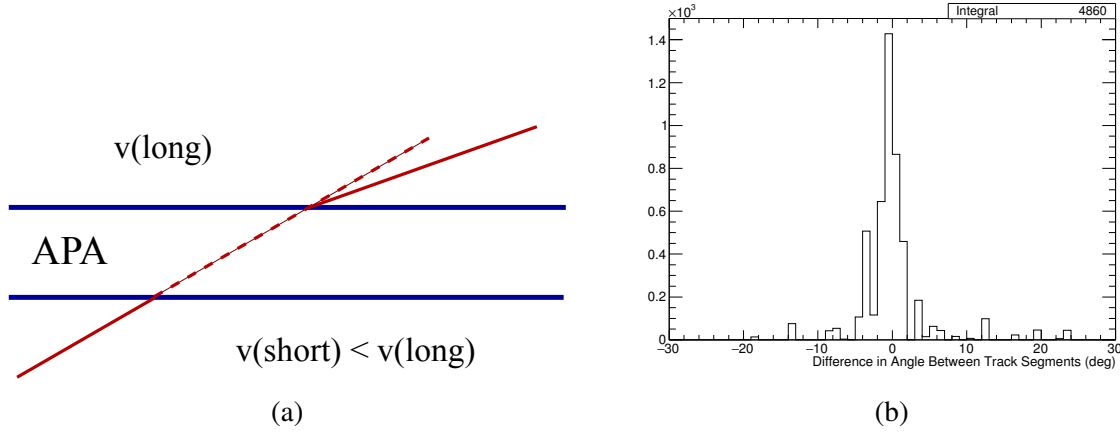


Fig. 7.24

collection plane for a given event should peak at zero if similar levels of noise were observed in each drift region; this is confirmed in Figure ??.

7.4 APA Gap-Crossing Muons

One of the primary motivations for the design of the 35 ton TPC was to test its modular form, where a single drift region is read out by multiple anode assemblies. Particles passing through the detector will inevitably leave deposits in multiple TPCs and will pass uninstrumented regions of the detector, such as gaps in between neighbouring APAs. An example such track is demonstrated schematically in Figure 7.25. It is essential the implications of this design choice are understood before constructing the far detector modules, each of which will contain 150 APAs.

The 35 ton dataset consisting of muons which pass across the face of APAs and therefore deposit charge in consecutive TPCs is discussed in this present section. An analysis of these tracks to calculate the size of the gaps is presented in Section 7.4.1 and a study of the charge deposited by such tracks is the subject of Section 7.4.2.

7.4.1 APA-Gap Offset Determination

It is possible to use these gap crossing tracks to make measurements of the gaps between each of the APAs. This involves aligning the track segments from neighbouring TPCs, demonstrated in Figure 7.26. The value of the z -offset, Δz , is determined by considering a range of offset hypotheses, performing a linear fit and finding the offset which minimises the

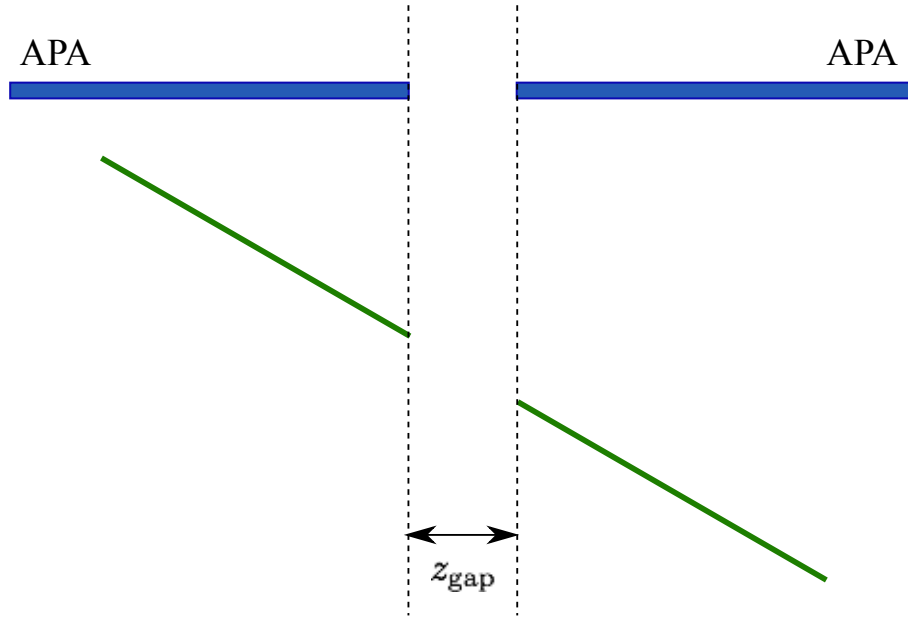


Fig. 7.25 Schematic showing an example APA-gap crossing track as viewed looking down from the top of the detector. The vertical direction represents the drift direction (x); the horizontal direction represents the z -direction. In general, these tracks make an angle with respect to the face of the APAs, as shown in the figure. As the gap in between the APAs is uninstrumented, no charge is desposited in this region.

residual least squares

$$L = \sum_i^{nhits} (o_i - e_i)^2, \quad (7.1)$$

where $o_i - e_i$ is the distance from hit i to the best fit line.

There are eight gaps which can be measured from the data, demonstrated in Figure ???. Due to very low statistics, it was found measurements of the gaps on the short drift volume side of the APAs were not possible using the 35 ton data. Analysis of the gaps using tracks passing through the long drift volume, hereafter named TPC1/TPC3, TPC1/TPC5, TPC3/TPC7 and TPC5/TPC7, was therefore the focus of this study.

A number of cuts were applied to ensure only high quality tracks were included for analysis:

- Only hits greater than 1 cm and less than 15 cm away from the gap were included in the track segments. The purpose of this cut is to limit the effect of multiple scatterings and the poorly understood region closest to the gap, where charge deposited in the uninstrumented region may later be collected.

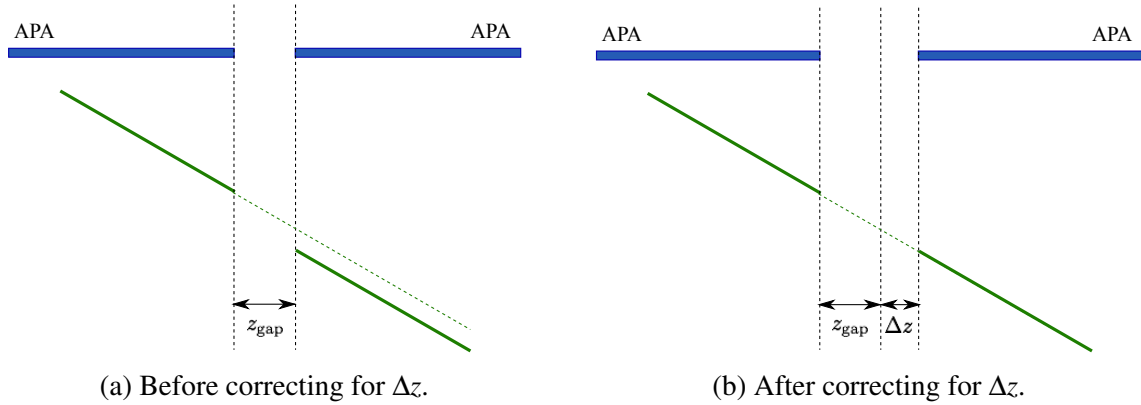


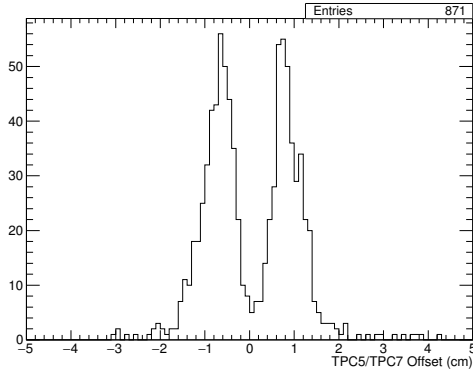
Fig. 7.26 Schematic showing an example track crossing two drift regions offset by an unknown quantity Δz . The effect of this is evident from the track desposits (Figure 7.26a) and can be corrected by ensuring the segments are aligned between the TPCs (Figure 7.26b).

- Each track segment must contain at least three hits to allow an accurate measure of the gradient.
- The angle between the track segments either side of the gap must be less than 2° to remove any poorly reconstructed tracks, or segments originating from different particle tracks.
- The angle the track makes with respect to the APA face must be large enough that the gap offset effect can be measured to an acceptable accuracy. It is common in the 35 ton to refer to a ‘counter gradient’, the offset between the two counters forming the through-going particle trigger in the drift direction, in units of counter length (refer to Figure ??). The tracks must have a counter gradient of at least three.

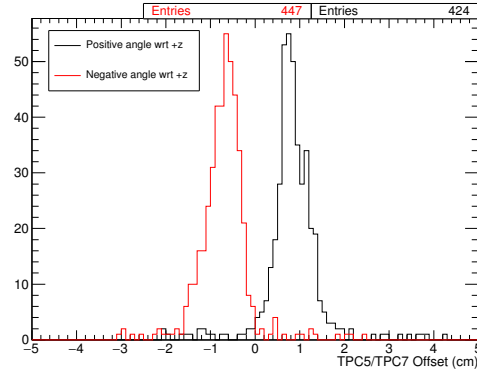
7.4.1.1 Measuring the APA Gaps

The gap with which we can expect the largest number of crossers is TPC5/TPC7 and so the method will be demonstrated using data from this channel. The z -offset determined using the method and cuts described above is shown in Figure 7.27. An unexpected feature is evident from this distribution; there is not a single peak but two, seemingly related to the angle which the through-going particle makes with respect to the APAs.

One explanation for this observed double-peak effect involves considering the possibility of additional offsets from the assumed positions of the APAs. This is demonstrated in Figure 7.28. It appears an offset in the x -position of the APAs could result in the problems encountered in the data. In order to test this, these offsets were artificially introduced into the simulation; the findings are presented in Figure 7.30. It appears the distribution of Δz



(a) Full distribution.



(b) Separated by the angle the track makes to the APAs.

Fig. 7.27 The z -offset for the TPC5/TPC7 gap measured in the 35 ton data. A very noticeable double-peak structure is evident in Figure 7.27a; this bias appears to be related to the sign of the angle the particle track makes to the APA planes.

measured from the data is consistent with APAs with offsets from expectation in both x and z . Moreover, it may be possible to measure both offsets from the same data set.

It is clear from Figure 7.30 that the z -offset may be determined as the minimum between the angular-separated distributions. This can be justified by geometrical considerations, explained in Figure 7.31. In this case, this may be achieved by fitting a function of the form

$$f(x) = a(x - b)^2 + c \quad (7.2)$$

and extracting parameter b as the true value of Δz . This is shown in Figure 7.32.

Using this measured value of Δz , the offsets can be analysed again, this time measuring the x -offset by correcting for the z -offset. The measured x -offset distribution is shown in Figure 7.33. With this value of Δx , the z -offset can be evaluated once more to ensure the distribution contains a single peak, as initially expected. This is confirmed in Figure 7.34.

7.4.1.2 Measurements of the APA Offsets

The offsets apparent from the data for all of the gaps accessible using TPC tracks in the long drift volume were determined as described in Section 7.4.1.1. Appendix ## contains all relevant figures (does an appendix seem a good idea here? I don't think we need the same figures as the previous section for each of the gaps here, but might be nice to have them somewhere?). Table 7.1 contains all the measurements and the new gaps, taking these offsets into account, are presented in Table ??.

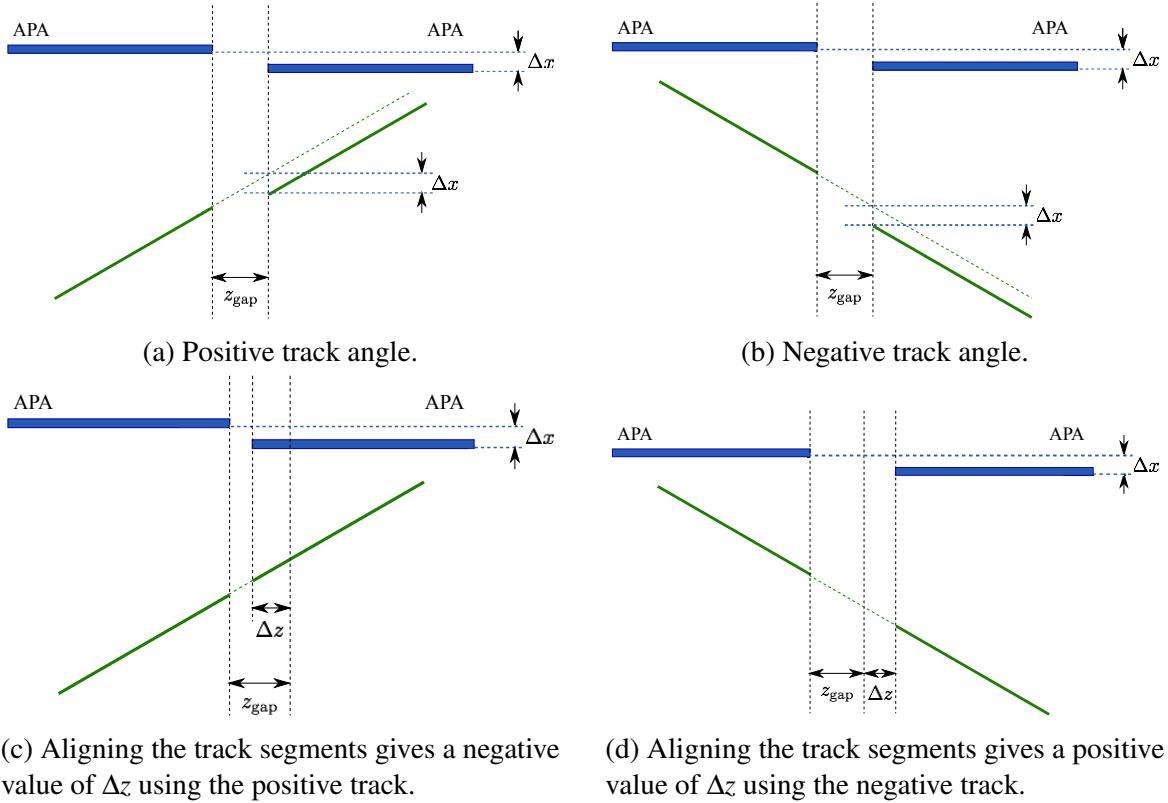


Fig. 7.28 Demonstration of how an x -offset in the positions of the APAs can explain the degeneracy evident in the z -offset measured using the 35 ton data (Figure 7.27). In the left-hand plots, Figures 7.28a and 7.28c, the through-going particle makes a positive angle to the face of the APAs and the right-hand plots, Figures 7.28b and 7.28d, the particle is travelling with a negative gradient. In both cases, the offset of the APAs in the x -direction is the same. It is clear from Figures 7.28c and 7.28d how the sign of the measured Δz is dependent on the angle of the track.

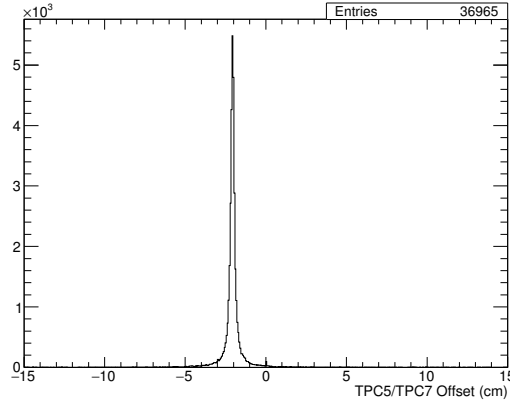
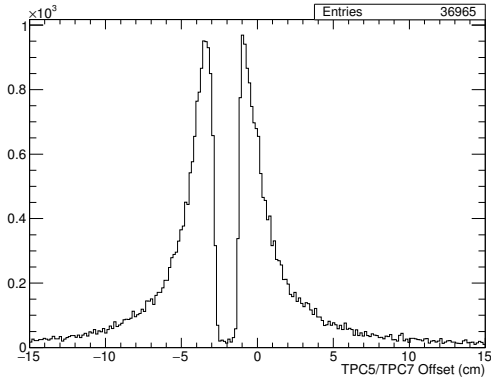
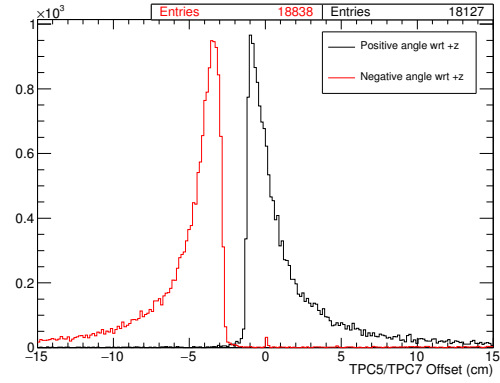
(a) z -offset = 2 cm, x -offset = 0 cm.(b) z -offset = 2 cm, x -offset = 0.5 cm.(c) z -offset = 2 cm, x -offset = 0.5 cm.

Fig. 7.29 Studies of the effects of offsets in the positions of the APAs in simulation. Artificial z - and x - offsets are introduced and their impact observed in the measurements of Δz . Figure 7.30a shows the effect of an offset in the z -direction; as expected, there is a single peak measuring the inputted value. Figures 7.30b and 7.30c show the consequence of offsets in both the x - and z -directions. This appears to show exactly what is seen in the 35 ton data (Figure 7.27).

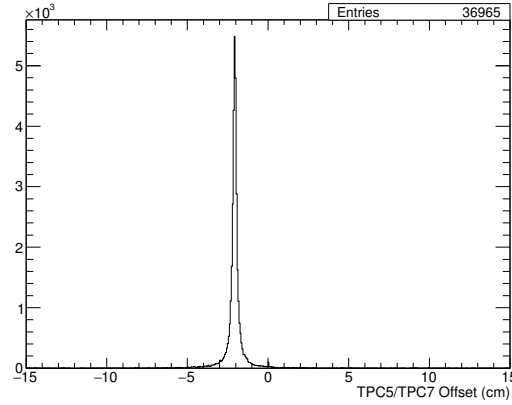
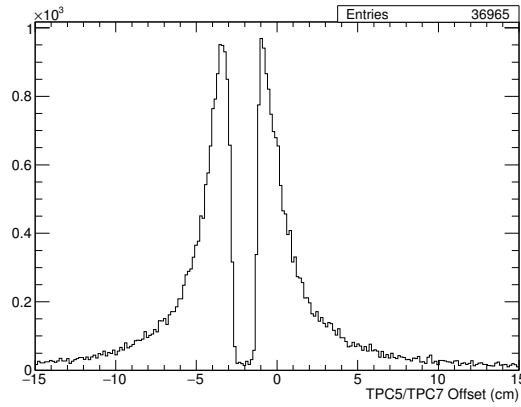
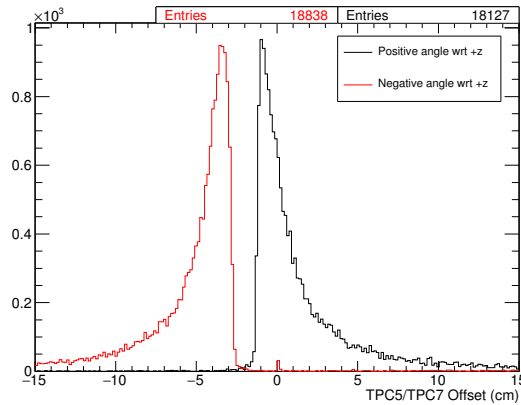
(a) z -offset = 2 cm, x -offset = 0 cm.(b) z -offset = 2 cm, x -offset = 0.5 cm.(c) z -offset = 2 cm, x -offset = 0.5 cm.

Fig. 7.30 [Same as previous page – which is better? I prefer the layout of the previous page but I like this one because you can see the 2cm offset in line with each other down the page!] Studies of the effects of offsets in the positions of the APAs in simulation. Artificial z - and x - offsets are introduced and their impact observed in the measurements of Δz . Figure 7.30a shows the effect of an offset in the z -direction; as expected, there is a single peak measuring the inputted value. Figures 7.30b and 7.30c show the consequence of offsets in both the x - and z -directions. This appears to show exactly what is seen in the 35 ton data (Figure 7.27).

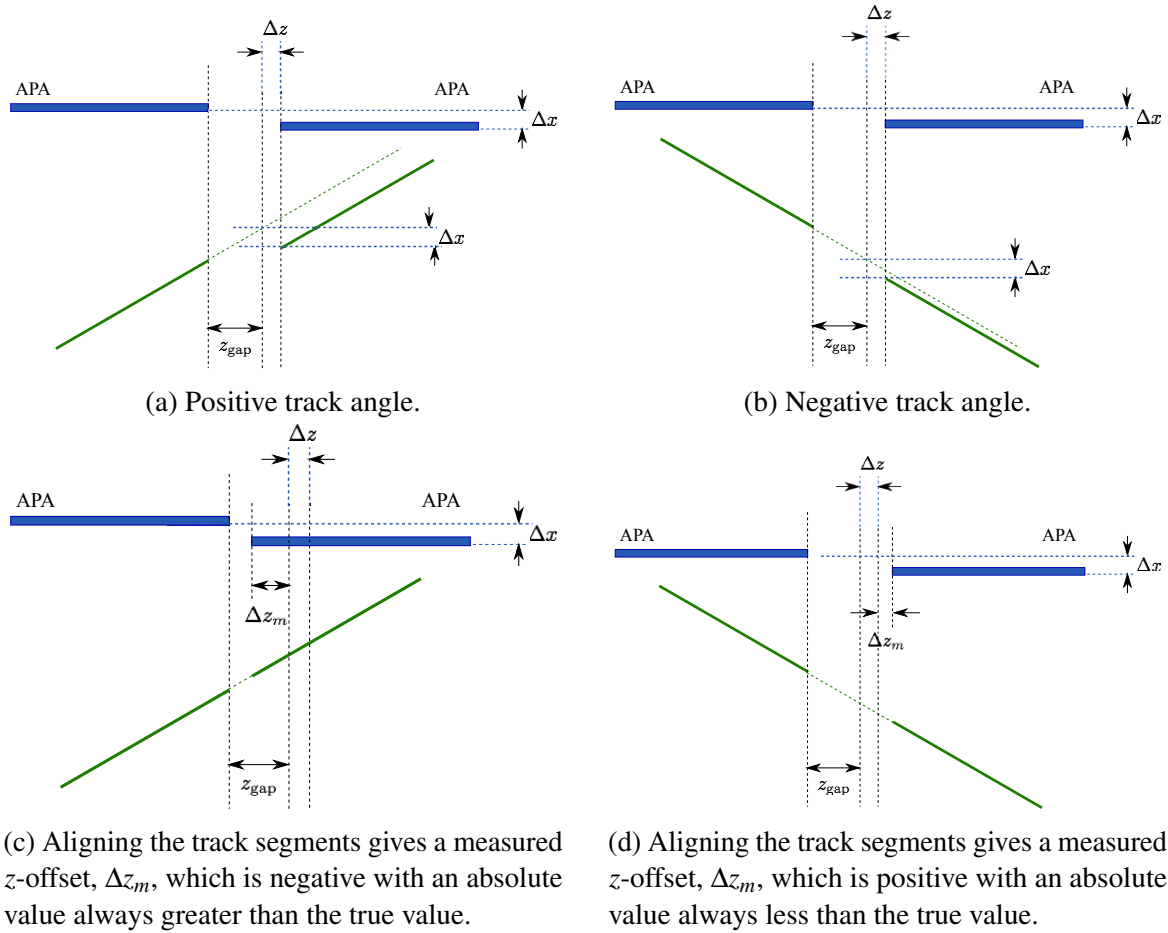


Fig. 7.31 Demonstration of the effects of offsets in both the x - and z -directions in the determination of Δz between TPC5 and TPC7. With an x -offset present, it is impossible for the true value of Δz to be measured – this is evident from Figure 7.30. It is clear from these geometrical considerations how the measured offset Δz_m will populate distributions either side of the true value; the true value Δz is given by the minimum between the two distributions.

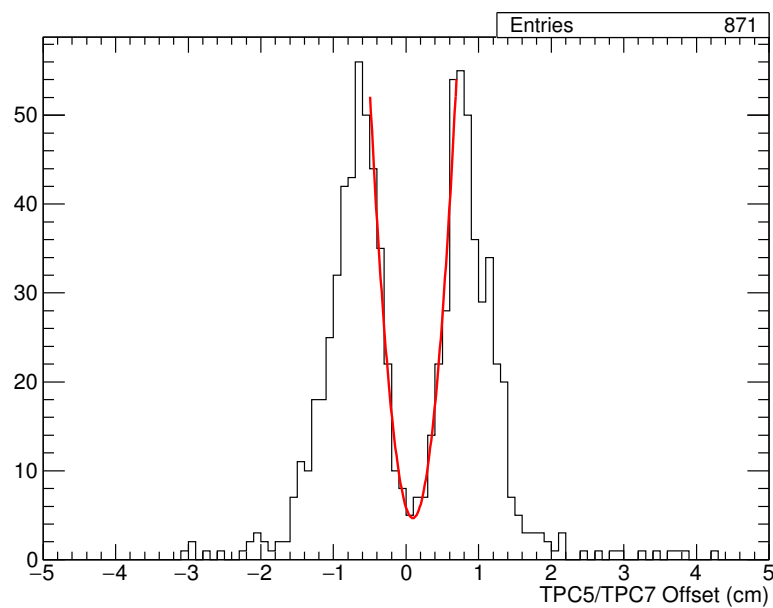


Fig. 7.32 Extraction of the true value of Δz from the full distribution of measured z -offsets. A measured value of 0.09 ± 0.02 cm is found.

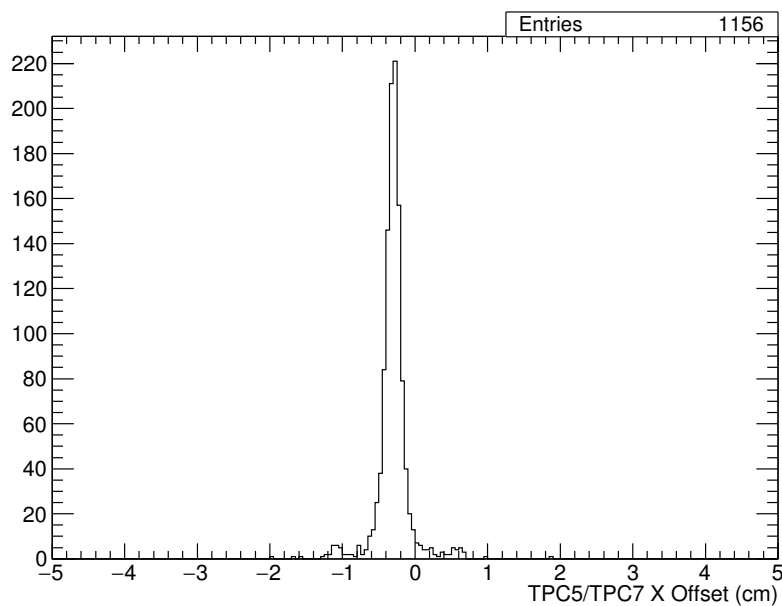


Fig. 7.33 Measurement of the x -offset between TPC5 and TPC7 after applying the z -gap corrected determined using the method described in the text and Figure 7.32. A measurement of -0.300 ± 0.003 cm is determined.

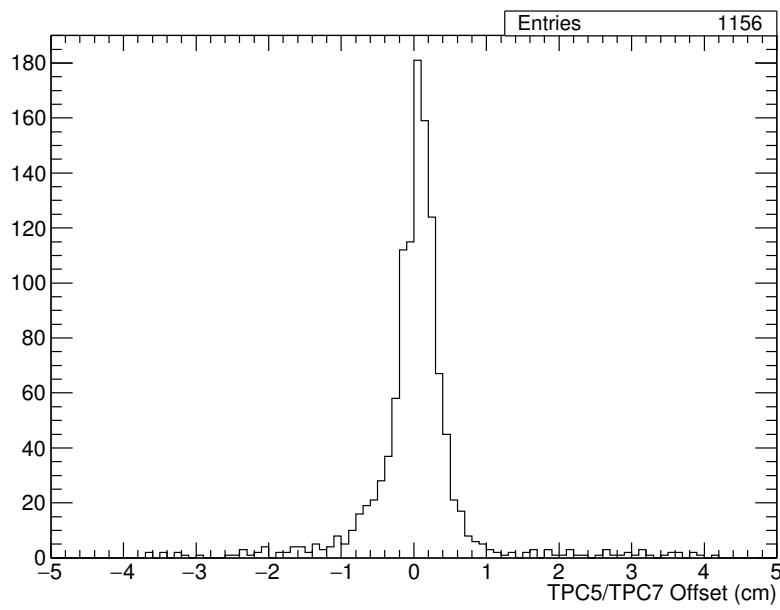


Fig. 7.34 Measurement of the z -offset between TPC5 and TPC7 after applying the x -offset determined from Figure 7.33. As initially anticipated, there is a single peak distributed around the true value of the offset. This validates the method used and confirms the initial presence of an x -offset between the neighbouring APAs. The final measurement of Δz is 0.057 ± 0.009 cm which agrees reasonably with the value measured previously (0.09 ± 0.02 cm from Figure 7.32).

Table 7.1 Measurements of all the APA offsets determined from the 35 ton TPC data. The method followed is described in Section 7.4.1.1. The first row represents the initial measurements of the z -offset from the two-peak distribution, with the following two lines detailing the measured offsets that follow from these results.

	TPC1/TPC3	TPC1/TPC5	TPC3/TPC7	TPC5/TPC7
Initial z -offset (cm)	-0.58 ± 0.08	0.18 ± 0.02	0.6 ± 0.1	0.09 ± 0.02
x -offset (cm)	-0.36 ± 0.01	-0.252 ± 0.006	-0.12 ± 0.02	-0.300 ± 0.003
z -offset (cm)	-0.57 ± 0.04	0.09 ± 0.02	0.55 ± 0.08	0.057 ± 0.009

Table 7.2 The corrected gaps between the APAs, in x and z , based on the offsets measured (Table 7.1).

	Assumed (cm)	Offset (cm)	Corrected (cm)
TPC1/TPC3 x -gap	0	-0.36 ± 0.01	-0.36 ± 0.01
TPC1/TPC5 x -gap	0	-0.252 ± 0.006	-0.252 ± 0.006
TPC3/TPC7 x -gap	0	-0.12 ± 0.02	-0.12 ± 0.02
TPC5/TPC7 x -gap	0	-0.300 ± 0.003	-0.300 ± 0.003
TPC1/(3)/TPC7 x -gap	0	-0.48 ± 0.02	-0.48 ± 0.02
TPC1/(5)/TPC7 x -gap	0	-0.552 ± 0.007	-0.552 ± 0.007
TPC1/TPC3 z -gap	2.53	-0.57 ± 0.04	1.96 ± 0.04
TPC1/TPC5 z -gap	2.08	0.09 ± 0.02	2.17 ± 0.02
TPC3/TPC7 z -gap	1.63	0.55 ± 0.08	2.18 ± 0.08
TPC5/TPC7 z -gap	2.08	0.057 ± 0.009	2.14 ± 0.01
TPC1/(3)/TPC7 z -gap	4.16	-0.02 ± 0.09	4.14 ± 0.09
TPC1/(5)/TPC7 z -gap	4.16	0.15 ± 0.02	4.31 ± 0.02

Discussion of these numbers.

7.4.2 Charge Deposited by APA-Gap Crossing Muons

7.5 Shower Reconstruction in 35 ton Data

References

- [1] Wolfgang Pauli. Open letter to the participants of the conference in Tübingen, 1930.
- [2] E Fermi. Trends to a Theory of beta Radiation. (In Italian). *Nuovo Cim.*, 11:1–19, 1934.
- [3] E Fermi. Versuch einer Theorie der β -Strahlen. I. *Zeitschrift für Physik*, 88(3):161–177, 1934.
- [4] F. Wilson. Fermi's Theory of Beta Decay. *American Journal of Physics*, 36(12):1150–1160, 1968.
- [5] G M Lewis. *Neutrinos*. Wykeham publications, London; Winchester, 1970.
- [6] C M G Lattes, et al. Processes Involving Charged Mesons. *Nature*, 159:694–697, 1947.
- [7] C M G Lattes, G P S Occhialini, and C F Powell. Observations on the Tracks of Slow Mesons in Photographic Emulsions. 1. *Nature*, 160:453–456, 486–492, 1947.
- [8] R Brown, et al. Observations With Electron Sensitive Plates Exposed to Cosmic Radiation. *Nature*, 163:82, 1949.
- [9] C L Cowan, et al. Large Liquid Scintillation Detectors. *Phys. Rev.*, 90(3):493–494, 1953.
- [10] F. Reines and C. L. Cowan. A proposed experiment to detect the free neutrino, 1953.
- [11] F. Reines and C. L. Cowan. Detection of the free neutrino. *Physical Review*, 92(3):830–831, 1953.
- [12] C L Cowan, et al. Detection of the Free Neutrino: a Confirmation. *Science*, 124(3212):103–104, 1956.
- [13] Raymond Davis Jr. and Don S Harmer. Attempt to observe the $\text{Cl}^{37}(\bar{\nu}e^-)\text{Ar}^{37}$ reaction induced by reactor antineutrinos. *Bull. Am. Phys. Soc.*, 4:217, 1959.
- [14] G Danby, et al. Observation of High-Energy Neutrino Reactions and the Existence of Two Kinds of Neutrinos. *Phys. Rev. Lett.*, 9(1):36–44, 1962.
- [15] M. L. Perl, et al. Evidence for anomalous lepton production in e^+e^- annihilation. *Physical Review Letters*, 35(22):1489–1492, 1975.
- [16] G J Feldman, et al. Inclusive Anomalous Muon Production in e^+e^- Annihilation. *Phys. Rev. Lett.*, 38(3):117–120, 1977.

- [17] J Burmester, et al. Anomalous muon production in e^+e^- annihilations as evidence for heavy leptons. *Physics Letters B*, 68(3):297–300, 1977.
- [18] D. DeCamp, et al. Determination of the number of light neutrino species. *Physics Letters B*, 231(4):519–529, 1989.
- [19] B Adeva, et al. A determination of the properties of the neutral intermediate vector boson Z^0 . *Physics Letters B*, 231(4):509–518, 1989.
- [20] M Z Akrawy, et al. Measurement of the Z^0 mass and width with the opal detector at LEP. *Physics Letters B*, 231(4):530–538, 1989.
- [21] P Aarnio, et al. Measurement of the mass and width of the Z^0 -particle from multi-hadronic final states produced in e^+e^- annihilations. *Physics Letters B*, 231(4):539–547, 1989.
- [22] S. Schael, et al. Precision electroweak measurements on the Z resonance. *Physics Reports*, 427(5-6):257–454, 2006.
- [23] K. Kodama, et al. Observation of tau neutrino interactions. *Physics Letters, Section B: Nuclear, Elementary Particle and High-Energy Physics*, 504(3):218–224, 2001.
- [24] H A Bethe. Energy Production in Stars. *Phys. Rev.*, 55(5):434–456, 1939.
- [25] John N Bahcall, Neta A Bahcall, and Giora Shaviv. Present Status of the Theoretical Predictions for the ^{37}Cl Solar-Neutrino Experiment. *Phys. Rev. Lett.*, 20(21):1209–1212, 1968.
- [26] John N. Bahcall, Aldo M. Serenelli, and Sarbani Basu. New Solar Opacities, Abundances, Helioseismology, and Neutrino Fluxes. *The Astrophysical Journal*, 621(1):L85–L88, 2005.
- [27] B. T. Cleveland, et al. Update on the measurement of the solar neutrino flux with the Homestake chlorine detector. *Nuclear Physics B (Proceedings Supplements)*, 38(1-3):47–53, 1995.
- [28] John N Bahcall, M H Pinsonneault, and G J Wasserburg. Solar models with helium and heavy-element diffusion. *Rev. Mod. Phys.*, 67(4):781–808, 1995.
- [29] J. N. Abdurashitov, et al. Results from SAGE (The Russian-American gallium solar neutrino experiment). *Physics Letters B*, 328(1-2):234–248, 1994.
- [30] P. Anselmann, et al. Solar neutrinos observed by GALLEX at Gran Sasso. *Physics Letters B*, 285(4):376–389, 1992.
- [31] W. Hampel, et al. GALLEX solar neutrino observations: Results for GALLEX IV. *Physics Letters, Section B: Nuclear, Elementary Particle and High-Energy Physics*, 447:127–133, 1999.
- [32] E. Gaisser, T. K.; Engel, R.; Resconi. *Cosmic Rays and Particle Physics*. Cambridge University Press, 1990.

- [33] T J Haines, et al. Calculation of Atmospheric Neutrino-Induced Backgrounds in a Nucleon-Decay Search. *Phys. Rev. Lett.*, 57(16):1986–1989, 1986.
- [34] K S Hirata, et al. Experimental study of the atmospheric neutrino flux. *Physics Letters B*, 205(2):416–420, 1988.
- [35] W Anthony Mann. Atmospheric neutrinos and the oscillations bonanza. *Int. J. Mod. Phys.*, A15S1:229–256, 2000.
- [36] B Pontecorvo. Neutrino Experiments and the Problem of Conservation of Leptonic Charge. *Sov. Phys. JETP*, 26:984–988, 1968.
- [37] V Gribov and B Pontecorvo. Neutrino astronomy and lepton charge. *Physics Letters B*, 28(7):493–496, 1969.
- [38] B Pontecorvo. Mesonium and anti-mesonium. *Sov. Phys. JETP*, 6:429, 1957.
- [39] D Casper, et al. Measurement of atmospheric neutrino composition with the IMB-3 detector. *Phys. Rev. Lett.*, 66(20):2561–2564, 1991.
- [40] R Becker-Szendy, et al. Electron- and muon-neutrino content of the atmospheric flux. *Phys. Rev. D*, 46(9):3720–3724, 1992.
- [41] Y Fukuda, et al. Atmospheric $\nu\mu$ ve ratio in the multi-GeV energy range. *Physics Letters B*, 335(2):237–245, 1994.
- [42] Y Fukuda, et al. Evidence for Oscillation of Atmospheric Neutrinos. *Phys. Rev. Lett.*, 81(8):1562–1567, 1998.
- [43] Q R Ahmad, et al. Direct Evidence for Neutrino Flavor Transformation from Neutral-Current Interactions in the Sudbury Neutrino Observatory. *Phys. Rev. Lett.*, 89(1):11301, 2002.
- [44] J N Bahcall. Solar Models and Solar Neutrinos. *Physica Scripta*, 2005(T121):46, 2005.
- [45] Ziro Maki, Masami Nakagawa, and Shoichi Sakata. Remarks on the Unified Model of Elementary Particles. *Progress of Theoretical Physics*, 28(5):870, 1962.
- [46] John N Bahcall, Concepción M Gonzalez-Garcia, and Carlos Pena-Garay. Before and After: How has the SNO NC measurement changed things? *Journal of High Energy Physics*, 2002(07):54, 2002.
- [47] A Yu. Smirnov. The MSW effect and solar neutrinos. In *Neutrino telescopes. Proceedings, 10th International Workshop, Venice, Italy, March 11-14, 2003. Vol. 1+2*, pages 23–43, 2003.
- [48] L Wolfenstein. Neutrino oscillations in matter. *Phys. Rev. D*, 17(9):2369–2374, 1978.
- [49] S P Mikheev and A Yu. Smirnov. Resonance Amplification of Oscillations in Matter and Spectroscopy of Solar Neutrinos. *Sov. J. Nucl. Phys.*, 42:913–917, 1985.
- [50] S P Mikheev and A Yu. Smirnov. Resonant amplification of neutrino oscillations in matter and solar neutrino spectroscopy. *Nuovo Cim.*, C9:17–26, 1986.

- [51] K Eguchi, et al. First Results from KamLAND: Evidence for Reactor Antineutrino Disappearance. *Phys. Rev. Lett.*, 90(2):21802, 2003.
- [52] T Araki, et al. Measurement of Neutrino Oscillation with KamLAND: Evidence of Spectral Distortion. *Phys. Rev. Lett.*, 94(8):81801, 2005.
- [53] Abhijit Bandyopadhyay, et al. The Solar neutrino problem after the first results from KamLAND. *Phys. Lett.*, B559:121–130, 2003.
- [54] Pedro Cunha de Holanda and A Yu. Smirnov. LMA MSW solution of the solar neutrino problem and first KamLAND results. *JCAP*, 0302:1, 2003.
- [55] G L Fogli, et al. Evidence for Mikheyev-Smirnov-Wolfenstein effects in solar neutrino flavor transitions. *Phys. Lett.*, B583:149–156, 2004.
- [56] Thomas Mannel. Theory and Phenomenology of CP Violation. *Nuclear Physics B - Proceedings Supplements*, 167:115–119, 2007.
- [57] Tommy Ohlsson, He Zhang, and Shun Zhou. Radiative corrections to the leptonic Dirac CP-violating phase. *Phys. Rev. D*, 87(1):13012, 2013.
- [58] Tommy Ohlsson, He Zhang, and Shun Zhou. Probing the leptonic Dirac CP-violating phase in neutrino oscillation experiments. *Physical Review D - Particles, Fields, Gravitation and Cosmology*, 87(5):1–8, 2013.
- [59] K Abe, et al. Physics potential of a long-baseline neutrino oscillation experiment using a J-PARC neutrino beam and Hyper-Kamiokande. *Progress of Theoretical and Experimental Physics*, 2015(5):053C02, 2015.
- [60] F Kaether, et al. Reanalysis of the Gallex solar neutrino flux and source experiments. *Physics Letters B*, 685(1):47–54, 2010.
- [61] J N Abdurashitov, et al. Measurement of the solar neutrino capture rate with gallium metal. III. Results for the 2002–2007 data-taking period. *Phys. Rev. C*, 80(1):15807, 2009.
- [62] B Aharmim, et al. Combined analysis of all three phases of solar neutrino data from the Sudbury Neutrino Observatory. *Phys. Rev. C*, 88(2):25501, 2013.
- [63] A Gando, et al. Reactor on-off antineutrino measurement with KamLAND. *Phys. Rev. D*, 88(3):33001, 2013.
- [64] R Wendell, et al. Atmospheric neutrino oscillation analysis with subleading effects in Super-Kamiokande I, II, and III. *Phys. Rev. D*, 81(9):92004, 2010.
- [65] M G Aartsen, et al. Determining neutrino oscillation parameters from atmospheric muon neutrino disappearance with three years of IceCube DeepCore data. *Phys. Rev. D*, 91(7):72004, 2015.
- [66] P Adamson, et al. Measurement of Neutrino and Antineutrino Oscillations Using Beam and Atmospheric Data in MINOS. *Phys. Rev. Lett.*, 110(25):251801, 2013.

- [67] P Adamson, et al. Electron Neutrino and Antineutrino Appearance in the Full MINOS Data Sample. *Phys. Rev. Lett.*, 110(17):171801, 2013.
- [68] K Abe, et al. Precise Measurement of the Neutrino Mixing Parameter θ_{23} from Muon Neutrino Disappearance in an Off-Axis Beam. *Phys. Rev. Lett.*, 112(18):181801, 2014.
- [69] P Adamson, et al. First measurement of muon-neutrino disappearance in NOvA. *Phys. Rev. D*, 93(5):51104, 2016.
- [70] M C Gonzalez-Garcia, Michele Maltoni, and Thomas Schwetz. Updated fit to three neutrino mixing: status of leptonic CP violation. *Journal of High Energy Physics*, 2014(11):52, 2014.
- [71] Ivan Esteban, et al. Updated fit to three neutrino mixing: exploring the accelerator-reactor complementarity. *Journal of High Energy Physics*, 2017(1):87, 2017.
- [72] F P An, et al. Observation of Electron-Antineutrino Disappearance at Daya Bay. *Phys. Rev. Lett.*, 108(17):171803, 2012.
- [73] J K Ahn, et al. Observation of Reactor Electron Antineutrinos Disappearance in the RENO Experiment. *Phys. Rev. Lett.*, 108(19):191802, 2012.
- [74] K Abe, et al. Observation of Electron Neutrino Appearance in a Muon Neutrino Beam. *Phys. Rev. Lett.*, 112(6):61802, 2014.
- [75] P Adamson, et al. First Measurement of Electron Neutrino Appearance in NOvA. *Phys. Rev. Lett.*, 116(15):151806, 2016.
- [76] K Abe and Others. First combined analysis of neutrino and antineutrino oscillations at T2K. 2017.
- [77] V N Aseev, et al. Upper limit on the electron antineutrino mass from the Troitsk experiment. *Phys. Rev. D*, 84(11):112003, 2011.
- [78] Ch Kraus, et al. Final results from phase II of the Mainz neutrino mass search in tritium β -decay. *The European Physical Journal C - Particles and Fields*, 40(4):447–468, 2005.
- [79] Planck Collaboration, et al. Planck 2013 results. XVI. Cosmological parameters. *Astronomy & Astrophysics*, 571:A16, 2014.
- [80] S. Amerio, et al. Design, construction and tests of the ICARUS T600 detector. *Nuclear Instruments and Methods in Physics Research, Section A: Accelerators, Spectrometers, Detectors and Associated Equipment*, 527(3):329–410, 2004.
- [81] C Anderson, et al. The ArgoNeuT detector in the NuMI low-energy beam line at Fermilab. *Journal of Instrumentation*, 7(10):P10019, 2012.
- [82] F Cavanna, et al. LArIAT: Liquid Argon In A Testbeam. 2014.
- [83] R Acciarri, et al. Design and construction of the MicroBooNE detector. *Journal of Instrumentation*, 12(02):P02017, 2017.

- [84] B Baller, et al. Liquid Argon Time Projection Chamber research and development in the United States. *Journal of Instrumentation*, 9(05):T05005, 2014.
- [85] David R Nygren. The Time Projection Chamber - A New 4pi Detector for Charged Particles. *eConf*, C740805(PEP-0144):58–78, 1974.
- [86] Carlo Rubbia. The Liquid Argon Time Projection Chamber: A New Concept For Neutrino Detectors.pdf, 1977.
- [87] Mitch Soderberg. The MicroBooNE Proposal, 2008.
- [88] V Chepel and H Araújo. Liquid noble gas detectors for low energy particle physics. *Journal of Instrumentation*, 8(04):R04001, 2013.
- [89] Terry Tope, et al. Extreme argon purity in a large, non-evacuated cryostat. 1169(2014):1169–1175, 2014.
- [90] A. Curioni, et al. A regenerable filter for liquid argon purification. *Nuclear Instruments and Methods in Physics Research, Section A: Accelerators, Spectrometers, Detectors and Associated Equipment*, 605(3):306–311, 2009.
- [91] Alan Hahn, et al. The LBNE 35 Ton Prototype Cryostat. In *FERMILAB-CONF-14-420-PPD The*, 2014.
- [92] David Montanari, et al. First scientific application of the membrane cryostat technology. 1664(2014):1664–1671, 2014.
- [93] J. Freeman. Courtesy of John Freeman, Fermilab, 2014.